ATLAS CONF Note

ATLAS-CONF-2020-003

26th February 2020

Search for new phenomena with top quark pairs in final states with one lepton, jets, and missing transverse momentum in pp collisions at $\sqrt{s} = 13$ TeV with the ATLAS detector

The ATLAS Collaboration

A search for new phenomena with top quark pairs in final states with one isolated electron or muon, multiple jets, and large missing transverse momentum is performed. Signal regions are employed to search for two- and four-body decays of the directly pair-produced supersymmetric partner of the top quark (stop). Additional signal regions are designed specifically to search for spin-0 mediator models, where the mediator is produced in association with a pair of top quarks and decays into a pair of dark matter particles. The search is performed using the Large Hadron Collider proton-proton dataset at a centre-of-mass energy of $\sqrt{s} = 13$ TeV recorded by the ATLAS detector from 2015 to 2018, corresponding to an integrated luminosity of 139 fb^{-1}. No significant excess from the Standard Model background is observed, and limits at 95% confidence level are set in the stop–neutralino and in the mediator–dark matter particle mass planes. Stops are excluded up to 1200 GeV in the two-body decay scenario. In the four-body scenario stops up to 640 GeV are excluded for a stop–neutralino mass difference of 60 GeV. Scalar and pseudo-scalar dark matter mediators are excluded up to 200 GeV when the coupling strengths of the mediator to standard model and dark matter particles are both equal to one and when the mass of dark-matter is 1 GeV.

ATLAS-CONF-2020-003
26 February 2020

1 Introduction

Supersymmetry (SUSY) [1–7] extends the Standard Model (SM) by introducing supersymmetric partners for every SM particle, which have identical quantum numbers except for a half-unit difference in spin. Searches for a light supersymmetric partner of the top quark, denoted as the top squark or stop, are of particular interest after the discovery of the Higgs boson [8, 9] at the Large Hadron Collider (LHC). Stops may largely cancel divergent loop corrections to the Higgs-boson mass [10–17], and thus, supersymmetry may provide an elegant solution to the hierarchy problem [18–21]. The superpartners of the left- and right-handed top quarks, $\tilde{t}_{\mathrm{L}}$ and $\tilde{t}_{\mathrm{R}}$, mix to form two mass eigenstates, $\tilde{t}_1$ and $\tilde{t}_2$, where $\tilde{t}_1$ is the lighter of the two. Significant mass-splitting between the $\tilde{t}_1$ and $\tilde{t}_2$ particles is possible due to the large top quark Yukawa coupling. A generic R-parity-conserving[1] minimal supersymmetric extension of the SM (MSSM) [7, 10, 22–24] predicts pair production of SUSY particles and the existence of a stable lightest supersymmetric particle (LSP). The mass eigenstates from the linear superposition of charged or neutral SUSY partners of the Higgs and electroweak gauge bosons (higgsinos, winos and binos) are called charginos $\tilde{\chi}^{\pm}_{1,2}$ and neutralinos $\tilde{\chi}^0_{1,2,3,4}$. The lightest neutralino ($\tilde{\chi}^0_1$), here assumed to be the LSP, may provide a potential dark matter (DM) candidate, because it is stable and only interacts weakly with ordinary matter [25, 26].

This paper presents a search for direct pair production of $\tilde{t}_1$ particles, in a final state with exactly one isolated charged lepton (electron or muon[2], henceforth referred to simply as 'lepton') from the decay of a W boson, high-p_{T} jets, and a significant amount of missing transverse momentum ($\vec{p}_{\mathrm{T}}^{\,\mathrm{miss}}$), the magnitude of which is referred to as $E_{\mathrm{T}}^{\mathrm{miss}}$, from the two weakly interacting LSPs that escape detection. Scenarios with on- and off-shell production of W bosons and top quarks in the stop decays are considered, leading to 2-, 3- and 4-body decays of the stop. Production of a spin-0 mediator in association with top quarks and subsequently decaying into a pair of DM particles is also searched for with a dedicated signal region.

Dedicated searches for direct $\tilde{t}_1$ pair production were recently reported by the ATLAS [27–30] and CMS [31–38] Collaborations. Previous ATLAS and CMS searches extend the limit on $\tilde{t}_1$ masses at 95% confidence level to 1.2 TeV in the two-body decay scenario and up to ~450 GeV in the three-body decay scenario. Searches for spin-0 mediators decaying into a pair of DM particles and produced in association with heavy-flavour quarks have also been reported by the ATLAS [27, 39] and CMS [40] Collaborations.

2 Signal models and search strategy

Two classes of physics models are targeted by this search, the production of $\tilde{t}_1$ pairs in simplified SUSY models [41–43] where the only light sparticles are $\tilde{t}_1$ and $\tilde{\chi}^0_1$, and simplified benchmark models for DM production that assume the existence of a spin-0 mediator particle that can be produced in association with two top quarks [39, 44] and decays into a pair of DM particles $\chi\bar{\chi}$.

The experimental signatures of stop pair production can vary dramatically, depending on the mass-splitting between $\tilde{t}_1$ and $\tilde{\chi}^0_1$. Figure 1 illustrates the two-, and four-body stop decays considered in this note. In the regime where $\Delta m_{\tilde{t}_1,\tilde{\chi}^0_1} = m(\tilde{t}_1) - m(\tilde{\chi}^0_1)$ is larger than the top quark mass m_{top}, the two-body decay $\tilde{t}_1 \to t + \tilde{\chi}^0_1$ dominates. At smaller $\Delta m_{\tilde{t}_1,\tilde{\chi}^0_1}$, the three-body decay $\tilde{t}_1 \to bW\tilde{\chi}^0_1$ dominates as long as

[1] A multiplicative quantum number, referred to as R-parity, is introduced in SUSY models, in order to conserve baryon and lepton number. R-parity is 1 (−1) for all SM (SUSY) particles.

[2] Electrons and muons from τ decays are included.

$\Delta m_{\tilde{t}_1,\tilde{\chi}_1^0}$ is larger than the sum of the b-quark and W-boson masses. At the smallest values of $\Delta m_{\tilde{t}_1,\tilde{\chi}_1^0}$ the dominant decay channel is the four-body decay $\tilde{t}_1 \to bff'\tilde{\chi}_1^0$. The stop is always assumed to decay promptly. Flavour-changing neutral current processes are not considered, therefore in each $\Delta m_{\tilde{t}_1,\tilde{\chi}_1^0}$ mass regime the dominant decay channel is assumed to have 100% branching ratio. The analysis targerted the $\tilde{t}_1 \to bW\tilde{\chi}_1^0$ using the full Run-2 data was published as a CONF note [45].

The searches for stops presented in this note use several signal regions dedicated to each of the decay channels $\tilde{t}_1 \to t + \tilde{\chi}_1^0$, and $\tilde{t}_1 \to bff'\tilde{\chi}_1^0$. The selections are optimised for given benchmark model points, and are binned in key variables to retain sensitivity to the widest possible range of $\tilde{t}_1$ and $\tilde{\chi}_1^0$ masses.

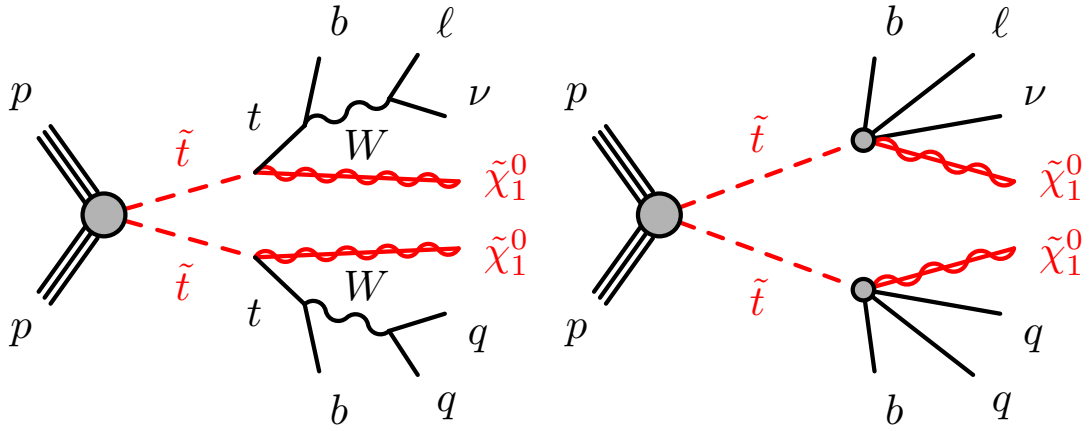

Figure 1: Diagrams illustrating the stop decay modes, which are referred to as (left) $\tilde{t}_1 \to t + \tilde{\chi}_1^0$ and (right) $\tilde{t}_1 \to bff'\tilde{\chi}_1^0$. Sparticles are shown as red lines. In these diagrams, the charge-conjugate symbols are omitted for simplicity. All considered processes involve the production of a squark–antisquark pair.

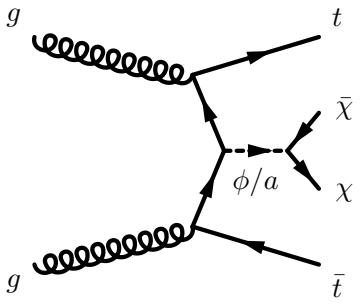

Figure 2: A representative Feynman diagram for spin-0 mediator production. The ϕ/a is the scalar/pseudoscalar mediator, which decays into a pair of dark matter (χ) particles.

The mediator-based DM scenarios consist of simplified models with a DM particle χ that is a SM singlet and a single spin-0 mediator that couples χ to SM fermions proportionally to the Yukawa interaction. Both scenarios where the mediator is a scalar, ϕ, or a pseudo-scalar, a are considered, as illustrated in Figure 2. These models have four parameters: the mass of the mediator m_{med}, the DM mass m_{DM}, the DM-mediator coupling g_χ, and the coupling of the mediator with the SM fermions g_{q}. In the models considered, the interaction between the mediator and SM particles is proportional to the fermion masses

via Yukawa-type couplings, therefore final states involving top quarks are important with respect to other fermions. Due to the associated production of top-quarks with undetected DM particles in the same event, the mediator-based DM model predicts an excess of $t\bar{t}+E_{\mathrm{T}}^{\mathrm{miss}}$ final state events above the SM expectation. A dedicated signal region common to both scalar and pseudo-scalar models is developed. The signal region is binned in the azimuthal angle $\Delta\phi(\vec{p}_{\mathrm{T}}^{\mathrm{miss}}, \ell)$ between the missing transverse momentum and the leading lepton, to retain maximum sensitivity to both scalar and pseudo-scalar models and to a large range of mediator and DM particle masses.

The searches presented are based on eight dedicated analyses that target the various scenarios mentioned above. Each of these analyses corresponds to a set of event selection criteria, referred to as a signal region (SR), and is optimised to allow for 3σ expected sensitivity of given benchmark models. Two techniques are employed to define the SRs: 'cut-and-count' and 'shape-fit' methods. The former is based on counting events in a single region of phase space, and is employed in the eight analyses. The latter is used in several SRs to improve the exclusion reach in case no excess is detected in the cut-and-count signal regions, and employs SRs split into multiple bins in one or two key discriminating kinematic variables. The shape-fit method exploits the varying signal-to-background ratios in different bins to provide sensitivity to a wider range of new particle masses than can be achieved by a single cut-and-count SR.

The main background processes after the signal selections include $t\bar{t}$, $t\bar{t}+Z(\rightarrow \nu\bar{\nu})$, W+jets and single-top Wt. These SM processes are estimated by building dedicated control regions (CRs) enhanced in the processes, making the analysis more robust against potential mis-modelling in simulated events and reducing the uncertainties in the background normalisation. The backgrounds are then normalised to data using a likelihood fit simultaneously to the SR and associated CRs. Prior to unblinding the signal regions, the background modelling and normalisation procedure are tested with a background-only fit to the CRs in a series of validation regions (VRs). After unblinding, a background-only fit to the CRs and SRs provides a statistical test that quantifies the existence and extent of a potential excess of events in data in the SRs. In absence of excess, exclusion limits are set on the associated model parameters based on theoretical cross-sections. An overview of the signal regions and the benchmark models for optimisation is presented in Table 1.

Table 1: Signal scenarios, benchmark models and signal regions. For each SR, the table lists the analysis technique used for exclusion limits. The last column points to the section where the signal region is defined. For `tN_high` no exclusion technique is defined. The `tN_med` shape-fit also covers the `tN_high`like phase space.

Signal scenario	Benchmark			Signal Region	Exclusion technique	Section
$\tilde{t}_1 \rightarrow t+\tilde{\chi}_1^0$	$m(\tilde{t}_1, \tilde{\chi}_1^0)$	=	(800,400) GeV	`tN_med`	shape-fit of $E_{\mathrm{T}}^{\mathrm{miss}}$ and m_{T}	7.1
$\tilde{t}_1 \rightarrow t+\tilde{\chi}_1^0$	$m(\tilde{t}_1, \tilde{\chi}_1^0)$	=	(950,1) GeV	`tN_high`	-	7.1
$\tilde{t}_1 \rightarrow t+\tilde{\chi}_1^0$	$m(\tilde{t}_1, \tilde{\chi}_1^0)$	=	(225,52) GeV	`tN_diag_low`	cut-and-count	7.2
$\tilde{t}_1 \rightarrow t+\tilde{\chi}_1^0$	$m(\tilde{t}_1, \tilde{\chi}_1^0)$	=	(500,327) GeV	`tN_diag_high`	cut-and-count	7.2
$\tilde{t}_1 \rightarrow bff'\tilde{\chi}_1^0$	$m(\tilde{t}_1, \tilde{\chi}_1^0)$	=	(500,450) GeV	`bffN_btag`	shape-fit in $p_{\mathrm{T}}^{\ell}/E_{\mathrm{T}}^{\mathrm{miss}}$ and $\Delta\phi(\vec{\mathrm{p}}_{\mathrm{T}}^{\mathrm{b-jet}}, \vec{p}_{\mathrm{T}}^{\mathrm{miss}})$	7.3
$\tilde{t}_1 \rightarrow bff'\tilde{\chi}_1^0$	$m(\tilde{t}_1, \tilde{\chi}_1^0)$	=	(450,430) GeV	`bffN_softb`	shape-fit in $p_{\mathrm{T}}^{\ell}/E_{\mathrm{T}}^{\mathrm{miss}}$	7.3
spin-0 mediator	$m(\phi/a, \chi)$	=	(20,1) GeV	`DM`	shape-fit in $\Delta\phi(\vec{p}_{\mathrm{T}}^{\mathrm{miss}}, \ell)$	7.4

3 ATLAS detector and data collection

The ATLAS experiment [46] at the LHC is a multi-purpose particle detector with almost 4π coverage in solid angle around the interaction point[3]. It consists of an inner tracking detector (ID) surrounded by a superconducting solenoid providing a 2 T axial magnetic field, electromagnetic and hadronic calorimeters, and a muon spectrometer (MS), which is based on three large air-core toroidal superconducting magnets. The ID provides charged-particle tracking in the range $|\eta| < 2.5$. During the LHC shutdown between Run 1 (2010–2012) and Run 2 (2015–2018), a new innermost layer of silicon pixels was added [47, 48], which improves the track impact parameter resolution, vertex position resolution and b-tagging performance [49]. High-granularity electromagnetic and hadronic calorimeters provide energy measurements up to $|\eta| = 4.9$. The electromagnetic calorimeters, as well as the hadronic calorimeters in the endcap and forward regions, are sampling calorimeters with liquid argon as the active medium and lead, copper, or tungsten absorbers. The hadronic calorimeter in the central region of the detector is a sampling calorimeter with scintillator tiles as the active medium and steel absorbers. The MS surrounds the calorimeters and is composed of three layers of precision tracking chambers with coverage up to $|\eta| = 2.7$ and fast detectors for triggering in the region $|\eta| < 2.4$. A two-level trigger system [50] is used in order to select events. The first-level trigger is hardware-based, followed by a software-based trigger system.

The results in this note utilise the full Run 2 dataset collected from 2015 to 2018 at a centre-of-mass energy of $\sqrt{s} = 13\,\text{TeV}$. The average number of simultaneous pp interactions per bunch crossing, referred to as "pile-up", in the recorded dataset is approximately 34. After the application of beam, detector and data-quality requirements, the total integrated luminosity is $139\,\text{fb}^{-1}$. The uncertainty in the combined 2015–2018 integrated luminosity is 1.7%. It is derived from the calibration of the luminosity scale using x-y beam-separation scans, following a methodology similar to that detailed in [51], and using the LUCID-2 detector for the baseline luminosity measurements [52].

All events were recorded with triggers that accept events with $E_{\text{T}}^{\text{miss}}$ above a given threshold. The $E_{\text{T}}^{\text{miss}}$ triggers rely on the energy mesurement in the calorimeter which is comprised of several algorithms based on cells, jets or topo-clusters in addition to two methods for correcting the effects of pile-up. The triggers are fully efficient for events passing an offline-reconstructed $E_{\text{T}}^{\text{miss}} > 230\,\text{GeV}$ requirement.

4 Simulated event samples

Samples of Monte Carlo simulated events are used for the description of the SM background processes and to model the signals. Details of the simulation samples used, including: the matrix element (ME) event generator and parton distribution function (PDF) set, the parton shower (PS) and hadronisation model, the set of tuned parameters (tune) for the underlying event (UE) and the order of the cross-section calculation, are summarised in Table 2.

The samples produced with MG5_aMC@NLO [68] and Powheg-Box [53, 75–78] used EvtGen v1.6.0 [79] for the modelling of b-hadron decays. The signal samples were all processed with a fast simulation [80],

[3] ATLAS uses a right-handed coordinate system with its origin at the nominal interaction point (IP) in the centre of the detector and the z-axis along the beam pipe. The x-axis points from the IP to the centre of the LHC ring, and the y-axis points upwards. Cylindrical coordinates (r, ϕ) are used in the transverse plane, ϕ being the azimuthal angle around the z-axis. The pseudorapidity is defined in terms of the polar angle θ as $\eta = -\ln\tan(\theta/2)$. The transverse momentum, p_{T}, is defined with respect to the beam axis (x–y plane).

Table 2: Overview of the nominal simulated samples. The cross-sections of top, single-top and SUSY samples were calculated at next-to-next-to-leading order (NNLO) with the resummation of soft gluon emission at next-to-next-to-leading-logarithm (NNLL) accuracy. The V+jets background samples were calculated at NNLO. The cross-sections of other background and DM samples were calculated at next-to-leading order (NLO).

Process	ME event generator	ME PDF	PS and hadronisation	UE tune	Cross-section calculation
$t\bar{t}$	Powheg-Box v2 [53]	NNPDF3.0 [54]	Pythia 8 [55]	A14 [56]	NNLO+NNLL [57–62]
Single-top					
t-channel	Powheg-Box v1	NNPDF3.0	Pythia 8	A14	NNLO+NNLL [63]
s- and Wt-channel	Powheg-Box v2	NNPDF3.0	Pythia 8	A14	NNLO+NNLL [64, 65]
V+jets ($V = W/Z$)	Sherpa 2.2.1 [66]	NNPDF3.0	Sherpa	Default	NNLO [67]
Diboson	Sherpa 2.2.1 – 2.2.2	NNPDF3.0	Sherpa	Default	NLO
Multiboson	Sherpa 2.2.1 – 2.2.2	NNPDF3.0	Sherpa	Default	NLO
$t\bar{t} + V$	MG5_aMC@NLO 2.3.3 [68]	NNPDF3.0	Pythia 8	A14	NLO [68]
SUSY signal	MadGraph 2.6.2 [68]	NNPDF2.3 [69]	Pythia 8	A14	NNLO+NNLL [70–72]
DM signal	MadGraph 2.6.2	NNPDF3.0	Pythia 8	A14	NLO [73, 74]

whereas all background samples were processed with the full simulation of the ATLAS detector [80] based on GEANT4 [81]. All samples were produced with varying numbers of minimum-bias interactions produced with Pythia 8 with the A3 tune [82] overlaid on the hard-scattering event to simulate the effect of multiple pp interactions in the same or nearby bunch crossings. The number of interactions per bunch crossing was reweighted to match the distribution in data.

The nominal $t\bar{t}$ sample and single-top sample cross-sections were calculated at NNLO with the resummation of soft gluon emission at NNLL accuracy and were generated with Powheg-Box (at NLO accuracy) interfaced to Pythia8 for parton showering and hadronisation. Additional $t\bar{t}$ samples were generated with MG5_aMC@NLO (at NLO accuracy)+Pythia8 and Powheg-Box+Herwig7 [83, 84] for modelling comparisons and evaluation of systematic uncertainties [85]. The $t\bar{t}$ and Wt processes have identical $WWbb$ final states and can interfere. The `tN_med` and `tN_high` regions receive significant contributions from both processes in a phase space where the interference is significant. Techniques used to model the interference such as diagram subtraction (DS) and diagram removal (DR) [86] were shown to provide an interval of predictions containing the data [87], but can lead to large uncertainties. Both schemes are investigated in this paper.

W+jets and Z+jets samples were generated with Sherpa v2.2.1 [66, 88] at NLO with up to two partons and up to four partons at LO. The production of diboson and multiboson [89] events was generated with Sherpa 2.2.1 – 2.2.2. For diboson, the production includes up to one parton at NLO and up to 3 partons at LO. For tri-boson processes up to two extra partons are considered at LO. The Sherpa samples used Comix [90] and OpenLoops [91], and were merged with the Sherpa parton shower [92] using the ME+PS@NLO prescription [93]. The W+jets and Z+jets events were further normalised to the NNLO cross-sections [67].

The $t\bar{t} + V$ samples were generated with MG5_aMC@NLO (at NLO accuracy) interfaced to Pythia8 for parton showering and hadronisation. The corresponding Monte Carlo tune and generator comparisons can be found in Ref. [94].

The SUSY samples were generated at leading order (LO) with MadGraph 2.6.2 including up to two extra partons, and interfaced to Pythia8 for parton showering and hadronisation. For the $\tilde{t}_1 \rightarrow t + \tilde{\chi}_1^0$

samples, the stop was decayed in Pythia8 using only phase space considerations and not the full ME. For the $\tilde{t}_1 \to bff'\tilde{\chi}_1^0$ samples the stops are decayed with MadSpin [95], interfaced with Pythia8 for the parton showering. MadSpin emulates kinematic distributions such as the mass of the $bW^{(*)}$ system to a good approximation without calculating the full ME.

The signal cross-sections for stop pair production were calculated to approximate next-to-next-to-leading order in the strong coupling constant, adding the resummation of soft gluon emission at next-to-next-to-leading-logarithmic accuracy (approximate NNLO+NNLL) [72, 96–98]. The nominal cross-section and the uncertainty were derived using the PDF4LHC15_mc PDF set, following the recommendations of Ref. [99]. The stop pair production cross-section varies from approximately 200 fb at $m_{\tilde{t}_1} = 600$ GeV to about 2 fb at $m_{\tilde{t}_1} = 1150$ GeV.

Signal events for the spin-0 scalar and pseudo-scalar mediator models were generated at LO with up to one additional parton with MadGraph 2.6.2 interfaced with Pythia8 for parton showering and hadronisation. In the DM sample generation the couplings of the mediator to the DM and SM particles (g_χ and g_q) were set to one. In Section 10 the experimental results are intepreted in terms of models with a single common coupling $g = g_\chi = g_q = 1$, and values of g lower than one are also considered. The kinematics of the mediator decay were found not to depend strongly on the values of the couplings, however the particle kinematic distributions are sensitive to the scalar or pseudo-scalar nature of the mediator and to the mediator and DM particle masses. The cross-sections were computed at NLO [73, 74] and decrease significantly when the mediator is produced off-shell. The production cross-section varies from approximately 26 pb to 130 fb for a 10 to 200 GeV scalar mediator and from approximately 600 fb to 120 fb for a 10 to 200 GeV pseudo-scalar mediator.

5 Event reconstruction

Events selected in the analysis must satisfy a series of beam, detector and data-quality criteria. The primary vertex, defined as the reconstructed vertex with the highest $\sum_{\text{tracks}} p_T^2$, must have at least two associated tracks with $p_T > 500$ MeV.

Depending on the quality and kinematic requirements imposed, reconstructed physics objects are labelled either as *baseline* or *signal*, where the latter is a subset of the former with tighter selection criteria required. Baseline objects are used when classifying overlapping selected objects and to compute the missing transverse momentum. Background contributions from $t\bar{t}$ and Wt production where both W-bosons decay leptonically, referred to as dileptonic $t\bar{t}$ or Wt events, are suppressed by vetoing events with more than one baseline lepton. Signal objects are used to construct kinematic and discriminating variables needed for the event selection.

Electron candidates are reconstructed from electromagnetic calorimeter cell clusters that are matched to ID tracks. Baseline electrons are required to have $p_T > 4.5$ GeV, $|\eta| < 2.47$, and to satisfy 'LooseAndBLayer' likelihood identification criteria that are following the methodology described in Ref. [100]. Furthermore, they must also satisfy a longitudinal impact parameter (z_0), defined as the distance from the point of closest approach between the track and the beam axis in the transverse plane to the primary vertex along the beam direction, where $|z_0 \sin\theta| < 0.5$ mm. Signal electrons must pass all baseline requirements and have a transverse impact parameter (d_0) that satisfies $|d_0|/\sigma_{d_0} < 5$, where σ_{d_0} is the uncertainty on d_0. Furthermore, signal electrons are required to be isolated. The isolation is defined as the sum of the transverse energy or momentum reconstructed in a cone with a certain size $\Delta R = \sqrt{\Delta\eta^2 + \Delta\phi^2}$ excluding

the energy of the electron itself. The isolation criteria rely on both track- and calorimeter-based information with a fixed requirement on the isolation energy divided by the electron's p_{T}. Electrons which pass the signal identification criteria, including the loose isolation, are called loose electrons. Tight electrons must in addition fullfill a tight electron likelihood identification criteria and pass a tight isolation.

Muon candidates are reconstructed from combined tracks that are formed from ID and MS tracks, or stand-alone MS tracks. Baseline muons up to $|\eta| = 2.7$ are used, and are required to have $p_{\mathrm{T}} > 4$ GeV, a longitudinal impact parameter $|z_0 \sin\theta| < 0.5$ mm, and to satisfy the 'Medium' identification criterion [101]. Signal muons must pass all baseline requirements and in addition have a transverse impact parameter $|d_0|/\sigma_{d_0} < 3$. Tight signal muons must pass tight isolation criteria, similar to those used for tight signal electrons, but with a fixed requirement on track-based isolation energy divided by the muon's p_{T}. A category of loose signal muons is also defined, which requires the 'Loose' identification criterion [101] and passes a looser isolation criterion.

Dedicated efficiency scale factors are derived from $Z \to \ell\bar{\ell}$ and $J/\psi \to \ell\bar{\ell}$ data samples to correct the simulations for minor mis-modelling of electron and muon identification, impact parameter and isolation selections. The p_{T} threshold of signal leptons is 25 GeV for electrons and muons in all signal regions except for signal regions dedicated to $\tilde{t}_1 \to bff'\tilde{\chi}_1^0$, where electrons with $p_{\mathrm{T}} > 4.5$ GeV and muons with $p_{\mathrm{T}} > 4$ GeV are used.

Jet candidates are built from topological clusters [102, 103] in the calorimeters using the anti-k_t algorithm [104] with a jet radius parameter $R = 0.4$ implemented in the FastJet package [105]. Jets are corrected for contamination from pile-up using the jet area method [106–108] and are then calibrated to account for the detector response [109, 110]. Jets in data are further calibrated according to *in situ* measurements of the jet energy scale [110]. Baseline jets are required to have $p_{\mathrm{T}} > 20$ GeV. Signal jets must have $|\eta| < 2.5$ and $p_{\mathrm{T}} > 25$ GeV in all signal regions, except in the four-body signal regions where the p_{T} threshold of signal jets is 20 GeV. Furthermore, signal jets with $p_{\mathrm{T}} < 120$ GeV and $|\eta| < 2.5$ are required to satisfy track-based criteria designed to reject jets originating from pile-up [108]. Events containing a signal jet that does not pass specific jet quality requirements ("jet cleaning") are vetoed from the analysis in order to suppress detector noise and non-collision backgrounds [111, 112]. The number of signal jets in an event is denoted N_{jet}. In addition to these jet candidates, the same anti-k_t algorithm is used to define larger radius (large-R) jets as discriminating variables for the top-quark reconstruction, as described in Section 6.

Jets identified as containing b-hadrons are referred to as b-tagged jets. Their identification is performed using the MV2c10 b-tagging algorithm, which examines quantities such as the impact parameters of associated tracks and characteristics of reconstructed secondary vertices [113, 114]. The algorithm is used at a working point that provides a 77% b-tagging efficiency in simulated $t\bar{t}$ events, and corresponds to a rejection factor of about 130 for jets originating from gluons and light-flavour quarks (light jets) and about 6 for jets induced by charm quarks. Corrections derived from data control samples are applied to account for differences between data and simulation for the efficiency and mis-tag rate of the b-tagging algorithm. The number of b-tagged jets in an event is denoted $N_{b\text{-jet}}$. Since MV2c10 is only applicable to baseline jets with $p_{\mathrm{T}} > 20$ GeV, it is not sensitive to low p_{T} b-hadrons. The presence of low transverse momentum b-hadrons, below 20 GeV, is instead inferred using a soft b-tagging algorithm, which does not rely on the presence of a calorimeter jet, but requires the presence of secondary vertices [115]. This technique is used to gain sensitivity to the $\tilde{t}_1 \to bff'\tilde{\chi}_1^0$ signal in the regime with $\Delta m_{\tilde{t}_1,\tilde{\chi}_1^0}$ lower than ~ 40 GeV. The number of secondary vertices in an event is denoted N_{SV}. Corrections derived from dedicated $t\bar{t}$ and

W+jets control regions are applied to the soft b-tagging efficiencies to account for differences between data and simulation.

Jets and associated tracks are also used to identify hadronically decaying τ leptons using the 'Loose' identification criterion described in Refs. [116, 117], which has a 85% (75%) efficiency for reconstructing τ leptons decaying into one (three) charged pions. The hadronic τ candidates are required to have one or three associated tracks, with total electric charge opposite to that of the signal electron or muon, $p_{\mathrm{T}} > 20$ GeV, and $|\eta| < 2.5$. The τ candidate p_{T} requirement is applied after a dedicated energy calibration [118, 119].

To avoid labelling the same detector signature as more than one object, an overlap removal procedure is applied. Given a set of baseline objects, the procedure checks for overlap based on either a shared track, ghost-matching [107], or a minimum distance[4] ΔR_y between pairs of objects. First, if a baseline lepton and a baseline jet are separated by $\Delta R_y < 0.2$, then the lepton is retained and the jet is discarded. Second, if a baseline jet and a baseline lepton are separated by $\Delta R_y < 0.4$, then the jet is retained and the lepton is discarded, in order to minimise the contamination of jets mis-identified as leptons. For the remainder of the paper, all baseline and signal objects are those that have passed the overlap removal procedure.

The missing transverse momentum $\vec{p}_{\mathrm{T}}^{\,\mathrm{miss}}$ is reconstructed from the negative vector sum of the transverse momenta of baseline electrons, muons, jets, and a soft term built from high-quality tracks that are associated with the primary vertex but not with the baseline physics objects [120, 121]. Photons and hadronically decaying τ leptons are not explicitly included but enter either as jets, electrons, or via the soft term.

6 Discriminating variables

The background processes contributing to a final state with one isolated lepton, jets and $E_{\mathrm{T}}^{\mathrm{miss}}$ are primarily semi-leptonic $t\bar{t}$ with one of the W-bosons decaying leptonically, and W+jets events with a leptonic decay of the W-boson. Both backgrounds can be efficiently reduced by requiring the transverse mass of the event, m_{T}, to be significantly larger than the W-boson mass. The transverse mass is defined as $m_{\mathrm{T}} = \sqrt{2p_{\mathrm{T}}^{\ell}E_{\mathrm{T}}^{\mathrm{miss}}[1-\cos(\Delta\phi)]}$, where $\Delta\phi$ is the azimuthal angle between the lepton and missing transverse momentum directions and p_{T}^{ℓ} is the transverse momentum of the charged lepton. Other discriminating variables used to distinguish signal from several categories of background events are described below.

6.1 Dileptonic $t\bar{t}$ reconstruction

The m_{T2} variable [122] is a generalisation of the transverse mass, applied to signatures where two particles are not directly detected. The variable m_{T2}^{τ} [123] is a variant of m_{T2} developed to identify and remove $t\bar{t}$ events where one W-boson decays to a hadronic τ candidate. In this case the τ-jet is used as the visible particle for one top branch and the observed electron or muon for the other top branch. For $t\bar{t}$ events where one W-boson decays leptonically and the other to a hadronic τ, m_{T2}^{τ} has an endpoint at the W-boson mass.

Dileptonic decays of $t\bar{t}$ events, where one lepton is not identified, constitute a significant background. The lost lepton can lead to to significant missing transverse momentum and also make the event evade an

[4] Rapidity $y \equiv 1/2\ln(E + p_z/E - p_z)$ is used instead of pseudorapidity (η) when computing the distance ΔR_y between objects in the overlap removal procedure.

m_{T2} requirement. The topness variable [124] quantifies how well an event can be reconstructed under a dileptonic top hypothesis and is defined as the logarithm of the minimum of the following quantity $\mathcal{S}$:

$$\begin{aligned}\mathcal{S}(p_{Wx}, p_{Wy}, p_{Wz}, p_{\nu z}) \quad = \quad & \frac{(m_W^2 - p_W^2)^2}{a_W^4} + \frac{(m_t^2 - (p_{b1} + p_\ell + p_\nu)^2)^2}{a_t^4} + \\ & \frac{(m_t^2 - (p_{b2} + p_W)^2)^2}{a_t^4} + \frac{(4m_t^2 - (\Sigma_i p_i)^2)^2}{a_{\mathrm{CM}}^4},\end{aligned} \tag{1}$$

under minimisation with respect to p_W and p_ν with the constraint $\vec{p}_{\mathrm{T},\nu} + \vec{p}_{\mathrm{T,W}} = \vec{p}_{\mathrm{T}}^{\,\mathrm{miss}}$. The quantity p_W represents the 4-vector of the W-boson for which the lepton was not reconstructed and is thus completely invisible. The quantities p_ℓ and p_ν are the lepton and neutrino 4-vectors from the W-boson whose lepton was identified. Finally p_{bi} refer to the two b-jets. The sum in the last term runs over the five assumed final state particles. If the event contains two b-tagged jets, the two permutations are tested in the minimisation. If the event has a single b-tagged jet then permutations where the second b-jet can be any of the two leading untagged jets are tested during the minimisation. The values of resolution parameters a_W, a_t and a_{CM} are constants taken from Ref. [124].

6.2 Reconstruction of hadronic top decays

Signal events contain one hadronic top decay $t \to q\bar{q}'b$, while such decays are absent from the dileptonic $t\bar{t}$ background. Therefore, reconstructing the hadronic top quark decay can provide additional discrimination against dileptonic $t\bar{t}$ events. A recursive reclustering jet algorithm searches for large radius jets such that the radius parameter R corresponds to the radius $R(p_{\mathrm{T}}) = 2 \times m_{\mathrm{top}}/p_{\mathrm{T}}$ expected from a hadronic top quark decay $t \to q\bar{q}'b$ [27]. The algorithm is based on the anti-k_t algorithm using signal jets as inputs and with initial radius parameter $R_0 = 3.0$. If a reclustered large radius jet is significantly narrower than the radius expected from a hadronic top quark decay of that p_{T}, it is discarded. The radius of the remaining reclustered jets is iteratively reduced until the radius approximately matches the radius expected from a hadronic top quark decay. Surviving reclustered jets constitute hadronic top candidates. If more than one hadronic top candidate is found, the candidate whose mass $m_{\mathrm{top}}^{\mathrm{reclustered}}$ is closest to m_{top} is retained.

A second hadronic top quark candidate algorithm is employed, which fully reconstructs the direction of both the leptonically and the hadronically decaying top quarks, respectively denoted t_{lep} and t_{had}. This algorithm is applied on events with at least four jets and one b-tagged jet. The m_{top}^{χ} variable is defined as the invariant mass of the triplet of signal jets, one of which must be b-tagged, most compatible with m_{top}, taking into account the jet momentum and energy resolution. The component of the $\vec{p}_{\mathrm{T}}^{\,\mathrm{miss}}$ perpendicular to t_{lep} in the $t\bar{t}$ rest frame, $E_{\mathrm{T},\perp}^{\mathrm{miss}}$, is small in semi-leptonic top quark decays since $\vec{p}_{\mathrm{T}}^{\,\mathrm{miss}}$ tends to align with the leptonically decaying top quark.

6.3 Backgrounds with mismeasured missing momentum

In some signal regions additional suppression against backgrounds with mismeasured missing momentum, arising from mismeasured jets, is needed. This additional rejection is provided by $H_{\mathrm{T,sig}}^{\mathrm{miss}} = (|\vec{H}_{\mathrm{T}}^{\mathrm{miss}}| - M)/\sigma_{|\vec{H}_{\mathrm{T}}^{\mathrm{miss}}|}$, where $\vec{H}_{\mathrm{T}}^{\mathrm{miss}}$ is the negative vectorial sum of the momenta of the signal jets and signal lepton [123]. The denominator is computed from the per-event jet energy uncertainties, while the lepton resolution is neglected. The offset parameter M is a characteristic scale of the background processes and is fixed at 100 GeV in this analysis.

6.4 Variables for compressed $\tilde{t}_1 \rightarrow t + \tilde{\chi}_1^0$

In order to discriminate stop pair production from the SM $t\bar{t}$ production, events are reconstructed according to both stop and semi-leptonic $t\bar{t}$ hypotheses.

The reconstruction of the event under the semi-leptonic $t\bar{t}$ hypothesis starts by looking for the hadronically decaying top quark candidate through the minimisation of the loss function:

$$L_t = \frac{(m_W^{\text{cand}} - m_W)^2}{m_W} + \frac{(m_{t_{\text{had}}}^{\text{cand}} - m_{\text{top}})^2}{m_{\text{top}}} \tag{2}$$

with m_W and m_{top} being the experimentally known W-boson and top quark masses. The W-boson candidate mass m_W^{cand} is either the mass of a single large anti-k_t jet with radius 1.0 or 1.2 or the invariant mass of two anti-k_t jets with radius 0.4. The hadronically decaying top quark candidate t_{had} is either one of the large-R jets or the W-boson candidate plus a b-tagged jet. The loss function is minimised over the jet permutations and the jet permutation at the minimum is retained as candidate constituents of the hadronic top. The visible part of the leptonically decaying top quark candidate ($t_{\text{lep}^{\text{vis}}}$) four-vector is determined by adding the four-vectors of the remaining highest-p_{T} b-tagged jet and of the signal lepton.

The reconstruction of the event under the stop hypothesis relies on the collinear approximation [125, 126], in which the top quark and the neutralino from the stop decay are collinear. This approximation is valid for compressed $\tilde{t}_1 \rightarrow t + \tilde{\chi}_1^0$ models ($\Delta m_{\tilde{t}_1, \tilde{\chi}_1^0} \approx 0$GeV) when a high-$p_{\text{T}}$ initial state radiation (ISR) jet in the event is required.

With this approximation and under a given value of the parameter $\alpha = m_{\tilde{\chi}_1^0}/m_{\tilde{t}_1}$, the four-vector $p^\mu(\alpha)$ of the neutrino can be calculated from the measured momenta of the hadronic and visible leptonic top quark candidates. The resulting $p^\mu(\alpha)$ is then used to compute the leptonically decaying W-boson's transverse mass m_{T}^α and the difference in m_{T} between the calculation under the hypothesis of a $t\bar{t}$ event and under the signal hypothesis, $\Delta m_{\text{T}}^\alpha = m_{\text{T}} - m_{\text{T}}^\alpha$. In the remainder of the paper, $\Delta m_{\text{T}}^\alpha$ denotes this variable evaluated at $\alpha = 0.135$, obtained from a stop mass of 200 GeV and $\tilde{\chi}_1^0$ mass of 27 GeV [27].

Since the mass of the stop in a compressed model is close to the sum of the top quark and neutralino masses, the parameter α can be approximated with $\alpha = m_{\tilde{\chi}_1^0}/(m_{\tilde{\chi}_1^0} + m_{t_{\text{had}}})$. Thus, given the measured value of $m_{t_{\text{had}}}^{\text{cand}}$, $m_{\tilde{\chi}_1^0}$ can be scanned to minimise the loss function:

$$L_\alpha = \frac{(m(\ell + \nu) - m_W)^2}{m_W} + \frac{(m(t_{\text{lep}^{\text{vis}}} + \nu) - m_{\text{top}})^2}{m_{\text{top}}} \tag{3}$$

where $m(\ell + \nu)$ is the invariant mass of the lepton and the neutrino ν, and $m(t_{\text{lep}^{\text{vis}}} + \nu)$ is the invariant mass of the leptonic top candidate and the neutrino ν. The neutrino four-vector is a function of a α. The value of $\Delta m_{\text{T}}^\alpha$ at the minimum of the loss function is labelled as $\Delta m_{\text{T}}^{\text{dyn}}$ and $m_{\tilde{\chi}_1^0}^{\text{dyn}}$ is used to denote the mass of the $\tilde{\chi}_1^0$ at the minimum of the loss function.

Under the collinear hypothesis, the neutrino momentum is fully known, however there is an ambiguity as to how the remaining missing transverse momentum is split between the two neutralinos. A third loss function is defined by:

$$L_{\tilde{t}_1} = \frac{\left(m_{\tilde{t}_1}^{\text{had}} - m_{\tilde{t}_1}\right)^2}{m_{\tilde{t}_1}} + \frac{\left(m_{\tilde{t}_1}^{\text{lep}} - m_{\tilde{t}_1}\right)^2}{m_{\tilde{t}_1}} \tag{4}$$

which compares the reconstructed leptonic and hadronic $\tilde{t}_1$ mass with a given $\tilde{t}_1$ mass hypothesis, $m_{\tilde{t}_1}$. The minimisation is performed with respect to the angles of the two neutralino momenta with the leptonically and hadronically decaying top quarks. As in Ref. [27], the loss function is evaluated for a stop mass of 200 GeV and $\tilde{\chi}_1^0$ mass of 27 GeV. The mass $m_{\tilde{t}_1}^{\text{lep}}$, which denotes the leptonic $\tilde{t}_1$ mass at the minimum of this loss function, takes lower and more peaked values for compressed $\tilde{t}_1 \to t + \tilde{\chi}_1^0$ models than for the SM top quark backgrounds. Finally, the fraction x_1 of hadronic top quark momentum over the parent stop momentum is also used to discriminate the stop signal over the background. The x_1 includes the projection of the vector of the momentum on the axis of the hadronically decaying top-quark. It is possible to take a negative value if the collinear assumption does not hold.

7 Signal regions

A preselection that exploits the basic characteristics of the signals is applied: the presence of a signal lepton, b-tagged jets and missing transverse momentum. The preselection is designed to have very high efficiency for the signal but to remove the most trivial backgrounds. In order to cover signals with both high momentum decay products such as in $\tilde{t}_1 \to t + \tilde{\chi}_1^0$ and low momentum decay products such as in $\tilde{t}_1 \to bff'\tilde{\chi}_1^0$, "soft-lepton" and "hard-lepton" preselections are defined and are presented in Table 3. All regions require $E_{\text{T}}^{\text{miss}} > 230$ GeV to ensure that the trigger is fully efficient. In order to reject multijet events with mismeasured jet momenta, a minimum azimuthal angular distance is imposed between the missing transverse momentum direction and the two leading jets, $\Delta\phi(j_{1,2}, \vec{p}_{\text{T}}^{\text{miss}}) > 0.4$.

The signal regions are then optimised using Monte Carlo event samples to maximise the expected discovery sensitivity for the targeted signals. A set of benchmark signal models, selected to cover the various stop and spin-0 mediator models, is used for optimisation. The optimisation is performed using an iterative algorithm, considering all studied discriminating variables and accounting for statistical and systematic errors in the evaluation of the discovery significance. An overview of the signal regions and the benchmark models for optimisation is presented in Table 1. The SRs are not designed to be orthogonal. The final exclusion limits are obtained by selecting at each point of the model parameter space the SR with the best expected sensitivity.

7.1 $\tilde{t}_1 \to t + \tilde{\chi}_1^0$

Two signal regions, `tN_med` and `tN_high`, are designed for models with $\Delta m_{\tilde{t}_1,\tilde{\chi}_1^0}$ significantly larger than m_{top}, and rely on large missing momentum and energetic jets. Selections on m_{T}, $H_{\text{T,sig}}^{\text{miss}}$, $E_{\text{T},\perp}^{\text{miss}}$ and topness are dictated by the need to suppress W+jets, $t\bar{t}$, and $t\bar{t} + V$ backgrounds. The presence of a hadronic top quark candidate with $m_{\text{top}}^{\text{reclustered}} > 150$ GeV is required primarily to ensure orthogonality with control regions. The `tN_med` and `tN_high` definitions are given in Table 4. A common exclusion region is defined by performing a two-variable shape-fit on the `tN_med` signal region, in case no excess is observed in the single bin discovery signal regions. The binning is designed to maximise the excluded parameter space in the $m_{\tilde{t}_1}$, $m_{\tilde{\chi}_1^0}$ plane. The two variables used for the binning are selected as the two most discriminating variables distinguishing between `tN_med` and `tN_high`, namely $E_{\text{T}}^{\text{miss}}$ and m_{T}. The resulting six bins are given in Table 4.

Table 3: Preselection criteria used for the hard lepton signal regions (left) and the soft lepton signal regions (right).

Selection		**hard-lepton**	**soft-lepton**
Trigger		$E_{\mathrm{T}}^{\mathrm{miss}}$ trigger	
Data quality		jet cleaning, primary vertex	
Second-lepton veto		no additional baseline leptons	
Number of leptons, tightness		= 1 'loose' lepton	= 1 'tight' lepton
Lepton p_{T}	[GeV]	> 25	$> 4(4.5)$ for $\mu(e)$
Number of jets	(jet p_{T})	≥ 4 (25 GeV)	≥ 1 (200 GeV) or ≥ 2 (20 GeV)
$E_{\mathrm{T}}^{\mathrm{miss}}$	[GeV]		> 230
$\Delta\phi(j_{1,2}, \vec{p}_{\mathrm{T}}^{\mathrm{miss}})$	[rad]		> 0.4
$N_{b\text{-jet}}$		≥ 1	–
m_{T}	[GeV]	> 30	–
m_{T2}^{τ}	[GeV]	> 80	–

7.2 Compressed $\tilde{t}_1 \to t + \tilde{\chi}_1^0$

The kinematics of the decay $\tilde{t}_1 \to t + \tilde{\chi}_1^0$ in the region where $\Delta m_{\tilde{t}_1, \tilde{\chi}_1^0} \approx m_{\mathrm{top}}$ differ significantly from the two signal regions defined above, and the stop signal is kinematically very similar to the $t\bar{t}$ process. This region of parameter space is referred to as the diagonal region. Two dedicated signal regions, `tN_diag_low` and `tN_diag_high` are designed to target scenarios on the diagonal, respectively for low mass and high mass stops. Both signal regions rely on the presence of a high-p_{T} initial state radiation (ISR) jet, which serves to boost the di-stop system. The signal region definitions are shown in Table 5 and are used both for exclusion and for discovery.

7.3 $\tilde{t}_1 \to bff'\tilde{\chi}_1^0$

The four-body decay $\tilde{t}_1 \to bff'\tilde{\chi}_1^0$ occurs when $\Delta m_{\tilde{t}_1, \tilde{\chi}_1^0}$ is smaller than the W-boson mass. In this scenario, the decay products have low momenta and often fall below the standard jet and lepton reconstruction p_{T} thresholds. It is therefore necessary to apply a soft-lepton preselection and require the presence of a high transverse momentum ISR jet, with $p_{\mathrm{T}} > 200$ GeV, in order to boost the momenta of the final state particles. A first four-body signal region, labelled as `bffN_btag`, is optimised following the requirement of the presence of at least one b-tagged jet. Because the b-tagged jets are required to have $p_{\mathrm{T}} > 20$ GeV, `bffN_btag` is not sensitive to $\Delta m_{\tilde{t}_1, \tilde{\chi}_1^0}$ below ~ 40 GeV. For this reason a second signal region, labelled as `bffN_softb`, is defined. This region does not rely on b-tagged jets but instead requires a soft b-tag identified by the presence of a secondary vertex. The `bffN_btag` signal region also exploits the correlation between the ISR jet p_{T} and $E_{\mathrm{T}}^{\mathrm{miss}}$ by cutting on the CT2 variable defined by $\mathrm{CT2} = \min(E_{\mathrm{T}}^{\mathrm{miss}}, p_{\mathrm{T}}^{\mathrm{ISR}} - 25\ \mathrm{GeV})$. The key variable used at the last stage of the selection is the ratio between the lepton momentum and the missing transverse momentum, $p_{\mathrm{T}}^{\ell}/E_{\mathrm{T}}^{\mathrm{miss}}$, which is bound to small values for the $\tilde{t}_1 \to bff'\tilde{\chi}_1^0$ signal and takes large values for the backgrounds. The exact definitions of the four-body signal regions are given in Table 6. For exclusion limits, the last selection, namely on $p_{\mathrm{T}}^{\ell}/E_{\mathrm{T}}^{\mathrm{miss}}$, is

Table 4: Event selections defining the signal regions `tN_med` and `tN_high`.

Selection		`tN_med`	`tN_high`
Preselection		hard-lepton preselection	
N_{jet}, $N_{b\text{-jet}}$		$\geq (4, 1)$	$\geq (4, 1)$
Jet p_{T}	[GeV]	$> (100, 90, 70, 50)$	$> (120, 50, 50, 25)$
$E_{\text{T}}^{\text{miss}}$	[GeV]	> 230	> 520
$E_{\text{T},\perp}^{\text{miss}}$	[GeV]	> 400	-
$H_{\text{T,sig}}^{\text{miss}}$		> 16	> 25
m_{T}	[GeV]	> 220	> 380
topness		> 9	> 8
$m_{\text{top}}^{\text{reclustered}}$	[GeV]	> 150	
$\Delta R(b, \ell)$		< 2.8	< 2.6
Exclusion technique		Based on shape-fit in $E_{\text{T}}^{\text{miss}}$ and m_{T} in `tN_med`	
Bin boundaries	[GeV]	$E_{\text{T}}^{\text{miss}} \in [230, 400]$, $m_{\text{T}} > 220$ $E_{\text{T}}^{\text{miss}} \in [400, 500]$, $m_{\text{T}} > 220$ $E_{\text{T}}^{\text{miss}} \in [500, 600]$, $m_{\text{T}} \in [220, 380]$ $E_{\text{T}}^{\text{miss}} \in [500, 600]$, $m_{\text{T}} > 380$ $E_{\text{T}}^{\text{miss}} > 600$, $m_{\text{T}} \in [220, 380]$ $E_{\text{T}}^{\text{miss}} > 600$, $m_{\text{T}} > 380$	

replaced by a shape fit. In the `bffN_softb`, the shape fit is performed in five bins of the variable $p_{\text{T}}^{\ell}/E_{\text{T}}^{\text{miss}}$ with bin boundaries $\{0, 0.015, 0.025, 0.04, 0.06, 0.08\}$. In the `bffN_btag` signal region the shape fit is performed in two variables, namely three bins in $p_{\text{T}}^{\ell}/E_{\text{T}}^{\text{miss}}$ with bin boundaries $\{0, 0.03, 0.06, 0.1\}$ and two bins in $\Delta\phi(p_{\text{T}}^{b-\text{jet}}, \vec{p}_{\text{T}}^{\text{miss}})$ with bin boundaries $\{0, 0.8, 1.5\}$.

7.4 Dark matter

The signal region optimisation to search for spin-0 mediator models favors a selection with at least two b-tagged jets and a leading b-tagged jet with $p_{\text{T}} > 80$ GeV. The distribution of $\Delta\phi(\vec{p}_{\text{T}}^{\text{miss}}, \ell)$ differentiates the scalar and pseudoscalar models from each other and also from the background. The resulting `DM_scalar` and `DM_pseudo` signal region definitions are given in Table 7. In addition to the above selections optimised for discovery, the exclusion sensitivity is maximised by relying on a shape fit in the region `DM_scalar` with the binning in $\Delta\phi(\vec{p}_{\text{T}}^{\text{miss}}, \ell)$ given in Table 7.

Table 5: Event selections defining the signal regions `tN_diag_low` and `tN_diag_high`.

Selection		`tN_diag_low`	`tN_diag_high`
Preselection		hard-lepton preselection without τ-veto	
N_{jet}, $N_{b\text{-jet}}$		$\geq$ (4, 1)	
Jet p_{T}	[GeV]	> (400, 40, 40, 40)	
m_{T}	[GeV]	> 150	> 110
$E_{\text{T}}^{\text{miss}}$	[GeV]	–	> 400
m_{T2}	[GeV]	–	< 360
$\Delta m_{\text{T}}^{\alpha}$	[GeV]	> 40	–
$\Delta m_{\text{T}}^{\text{dyn}}$	[GeV]	–	> 60
$m_{\tilde{t}_1}^{\text{lep}}$	[GeV]	< 600	–
$m_{\tilde{\chi}_1^0}^{\text{dyn}}$	[GeV]	> 5	[220, 595]
x_1		–	> −0.2
Exclusion technique		cut-and-count	

Table 6: Event selections defining the signal regions `bffN_softb` and `bffN_btag`.

Selection		`bffN_softb`	`bffN_btag`
Preselection		soft-lepton preselection	
N_{jet}		$\geq$ 1	$\geq$ 2
Jet p_{T}	[GeV]	> 200	
$N_{b\text{-jet}}$		=0	$\geq$ 1
b-jet p_{T}	[GeV]	–	< 50
N_{SV}		$\geq$ 1	–
m_{T}	[GeV]	> 90	
$E_{\text{T}}^{\text{miss}}$	[GeV]	> 250	–
$\Delta\phi(\vec{p}_{\text{T}}^{\text{miss}}, \ell)$	[rad]	< 2.0	–
CT2	[GeV]	–	> 400
$\Delta\phi(p_{\text{T}}^{b-\text{jet}}, \vec{p}_{\text{T}}^{\text{miss}})$	[rad]	–	< 1.5
$p_{\text{T}}^{\ell}/E_{\text{T}}^{\text{miss}}$		< 0.04	< 0.05
Exclusion technique		shape-fit in $p_{\text{T}}^{\ell}/E_{\text{T}}^{\text{miss}}$	shape-fit in $p_{\text{T}}^{\ell}/E_{\text{T}}^{\text{miss}}$ and $\Delta\phi(p_{\text{T}}^{b-\text{jet}}, \vec{p}_{\text{T}}^{\text{miss}})$
Bin boundaries in $p_{\text{T}}^{\ell}/E_{\text{T}}^{\text{miss}}$		{0, 0.015, 0.025, 0.04, 0.06, 0.08}	{0, 0.03, 0.06, 0.1}
Bin boundaries in $\Delta\phi(p_{\text{T}}^{b-\text{jet}}, \vec{p}_{\text{T}}^{\text{miss}})$	[rad]		{0, 0.8, 1.5}

Table 7: Event selections defining the DM signal regions.

Selection		DM_scalar	DM_pseudo
Preselection		hard-lepton preselection	
N_{jet}, $N_{b\text{-jet}}$		$\geq (4, 2)$	
Jet p_{T}	[GeV]	$>$ (80, 60, 30, 25)	
b-tagged jet p_{T}	[GeV]	$>$ (80, 25)	
$E_{\text{T}}^{\text{miss}}$	[GeV]	> 230	
$H_{\text{T,sig}}^{\text{miss}}$		> 15	
m_{T}	[GeV]	> 180	
topness		> 8	
$m_{\text{top}}^{\text{reclustered}}$	[GeV]	> 150	
$\Delta\phi(\text{jet}_i, \vec{p}_{\text{T}}^{\text{miss}})$, $i \in [1, 4]$	[rad]	> 0.9	
$\Delta\phi(\vec{p}_{\text{T}}^{\text{miss}}, \ell)$	[rad]	> 1.1	> 1.5
Exclusion technique		Based on shape fit in $\Delta\phi(\vec{p}_{\text{T}}^{\text{miss}}, \ell)$	
Bin boundaries in $\Delta\phi(\vec{p}_{\text{T}}^{\text{miss}}, \ell)$		$\{1.1, 1.5, 2.0, 2.5, \pi\}$	

8 Backgrounds

Data can be used to constrain the normalisation of the most significant background processes. To this end, control regions (CRs) are defined by minimally modifying the SR selections to suppress the signal while enhancing the fraction of the targeted background process. The CRs are then incorporated into a simultaneous likelihood fit to constrain the background process normalisations in the signal region. The relation between the number of background events of a given process in the SR and a CR is set by the MC within systematic uncertainties. Small background processes, such as diboson production and Z+jets, are always estimated directly from Monte Carlo simulation since they typically represent only a few percent of the signal region yields. CRs are defined to normalise $t\bar{t}$ (TCR), W+jets (WCR), single-top (STCR) and $t\bar{t}+Z$ (TZCR). Whether a control region is defined for a given background and signal region depends on the relative contribution of the process to the SR yield.

In order to validate the background estimates from the CRs, validation regions (VRs) are introduced for $t\bar{t}$ (TVR) and W+jets (WVR). The VRs are disjoint from both the SRs and CRs. The TZCR is designed to come as close as possible to the signal region, in order to maximise the precision on the estimate of the large $t\bar{t}+Z$ background and thus does not leave space between the SR and the CR to introduce a VR for this process. Background normalisations, referred as normalisation factors (NF), determined in the CRs are applied to the VRs and compared with the data. The VRs are not included in the final simultaneous fit, but provide a statistically independent test of the background estimates in background dominated regions. The potential signal contamination in the VRs is studied and required to be negligible compared to the total number of background events expected in the VRs. The CRs and VRs used for each SR are summarised in Table 8. If a processes is not normalised via a control region then it is estimated directly from Monte Carlo simulation and theoretical cross-sections.

Table 8: Summary of the control and validation regions used (✓) for each signal region.

Signal Region	Signal Scenario	TCR	WCR	STCR	TZCR	TVR	WVR
`tN_med`	$\tilde{t}_1 \to t + \tilde{\chi}_1^0$	✓	✓	✓	✓	✓	✓
`tN_high`	$\tilde{t}_1 \to t + \tilde{\chi}_1^0$	✓	✓	✓	✓	✓	✓
`tN_diag_low`	$\tilde{t}_1 \to t + \tilde{\chi}_1^0$	✓	–	–	–	✓	–
`tN_diag_high`	$\tilde{t}_1 \to t + \tilde{\chi}_1^0$	✓	–	–	–	✓	–
`bffN_btag`	$\tilde{t}_1 \to bff'\tilde{\chi}_1^0$	✓	✓	–	–	✓	✓
`bffN_softb`	$\tilde{t}_1 \to bff'\tilde{\chi}_1^0$	✓	✓	–	–	✓	✓
`DM`	spin-0 mediator	✓	–	–	✓	✓	–

8.1 Control and validation regions for $\tilde{t}_1 \to t + \tilde{\chi}_1^0$ and spin-0 mediator signals

The dominant background process in the tN_med, tN_high and DM signal regions is $t\bar{t} + Z$, therefore each of these SRs uses a dedicated TZCR. The TZCRs aim at capturing $t\bar{t} + Z$ events where the Z-boson decays to two electrons or muons, and thus is kinematically similar to the $t\bar{t} + Z$ background in the signal regions where the Z-boson decays to a pair of neutrinos. This CR is built by selecting events with three leptons (electrons or muons), one pair of which must be of opposite charge and same flavour with an invariant mass within 10 GeV of the Z-boson mass. The exact definitions of the TZCRs follow the definitions of the tN_med, tN_high and DM SRs in terms of the number of jets, b-tagged jets and jet p_{T} thresholds. The remaining SR selections are not applied to the TZCRs, in order to retain enough statistics. A modified missing momentum variable, $\tilde{E}_{\mathrm{T}}^{\mathrm{miss}}$, is defined, where the leptons associated to the Z-boson decay are considered invisible.

The W+jets and dileptonic $t\bar{t}$ processes are significant in tN_med and tN_high, therefore dedicated CRs, WCR and TCR, are employed. The DM signal region also employs a TCR but does not require a WCR due to the smaller size of the W+jets background. These CRs follow the number of jets, number of b-tagged jets and jet p_{T} thresholds as listed in Tables 4 and 7 for their respective signal regions. Table 9 presents the definitions of the TCRs, WCRs and VRs, by showing which selections are modified compared to the tN_med and tN_high SRs definitions. Neither W+jets, nor dileptonic $t\bar{t}$ processes yield hadronic top decays, therefore a veto on the presence of a hadronic reclustered top candidate is used to ensure orthogonality with the signal regions. The number of events in TCR and WCR is increased by relaxing several selections with respect to the SR selections. The $H_{\mathrm{T,sig}}^{\mathrm{miss}}$ selection is lowered to 10 for both tN_med and tN_high, and to 13 for DM. In addition, $E_{\mathrm{T},\perp}^{\mathrm{miss}}$ is lowered to 300 GeV for tN_med, while $E_{\mathrm{T}}^{\mathrm{miss}}$ is lowered to 450 GeV for tN_high. In the DM signal region the cut on $\Delta\phi(\mathrm{jet}_i, \vec{p}_{\mathrm{T}}^{\mathrm{miss}})$ is lowered to 0.6.

The topness and m_{T} selections are used to differentiate between WCR and TCR. In the WCR, m_{T} is required to be in the range 30–90 GeV, compatible with the presence of a semi-leptonic W decay, but incompatible with dileptonic $t\bar{t}$ thanks to the topness selection. In the TCR, the topness selection of the SR is inverted, thus selecting events compatible with dileptonic $t\bar{t}$, while m_{T} larger than 120 GeV is required, as larger values are favoured by the presence of two leptonically decaying W-bosons. The TCR dedicated to the DM signal region keeps the same m_{T} selection as its signal region, $m_{\mathrm{T}} > 180$ GeV. The purity of the WCR is further improved by using only positively charged leptons, exploiting the lepton charge asymmetry in W+jets events.

In order to validate the dileptonic $t\bar{t}$ background normalisation, a TVR dominated by $t\bar{t}$ production is designed. The TVRs for tN_med and tN_high have the same selections as the corresponding TCR, with the exception of the veto on the presence of a hadronic reclustered top quark candidate, which is replaced by the requirement of the presence of such a hadronic top quark, with a mass $m_{\mathrm{top}}^{\mathrm{reclustered}} > 150$ GeV.

The validation of the W+jets background for tN_high is performed with a WVR with the same selection as tN_high but requiring the presence of a hadronic reclustered top candidate with $m_{\mathrm{top}}^{\mathrm{reclustered}} > 150$ GeV and $H_{\mathrm{T,sig}}^{\mathrm{miss}} > 25$, in order to be closer to the SR. The WVR for tN_med is defined starting from the WCR selections, but replacing several selections with those used in its SR: $E_{\mathrm{T}}^{\mathrm{miss}} > 400$ GeV, $H_{\mathrm{T,sig}}^{\mathrm{miss}} > 16$ and the presence of a hadronic top quark, with a mass $m_{\mathrm{top}}^{\mathrm{reclustered}} > 150$ GeV.

The DM SR contains only a small fraction of W+jets events due to the requirement of two b-tagged jets, therefore only a TVR is considered. It is constructed from the DM SR definition, but with the topness

Table 9: Event selections defining the CRs and VRs in tN_med, tN_high and DM compared to their respective signal region.

Selection		tN_med	tN_med-TCR (-TVR)	tN_med-WCR (-WVR)	tN_med-STCR
$m_{\text{top}}^{\text{reclustered}}$	[GeV]	> 150	veto (> 150)	veto (> 150)	veto
$H_{\text{T,sig}}^{\text{miss}}$		> 16	> 10	> 10 (> 16)	> 10
$E_{\text{T},\perp}^{\text{miss}}$	[GeV]	> 400	> 300	> 300 (>400)	350
m_{T}	[GeV]	>220	>120	$\in [30, 90]$	$\in [30, 120]$
topness		> 9	< 9	> 9	> 10
$\Delta R(b, \ell)$		< 2.8	–	–	–
$\Delta R(b_1, b_2)$		–	–	< 1.4	> 1.4
Lepton charge		–	–	>0	–
$N_{b\text{-jet}}$		≥ 1	≥ 1	≥ 1	≥ 2
Selection		tN_high	tN_high-TCR (-TVR)	tN_high-WCR (-WVR)	tN_high-STCR
$m_{\text{top}}^{\text{reclustered}}$	[GeV]	> 150	veto (> 150)	veto (> 150)	veto
$H_{\text{T,sig}}^{\text{miss}}$		> 25	> 10	> 10 (> 25)	> 10
$E_{\text{T}}^{\text{miss}}$	[GeV]	> 520	> 450	> 450	> 450
m_{T}	[GeV]	>380	>120	$\in [30, 90]$	$\in [30, 120]$
topness		> 8	< 8	> 8	> 10
$\Delta R(b, \ell)$		< 2.6	–	–	–
$\Delta R(b_1, b_2)$		–	–	< 1.4	> 1.4
Lepton charge		–	–	>0	–
$N_{b\text{-jet}}$		≥ 1	≥ 1	≥ 1	≥ 2
Selection		DM	DM-TCR (-TVR)		
$m_{\text{top}}^{\text{reclustered}}$	[GeV]	> 150	veto (> 150)		
$H_{\text{T,sig}}^{\text{miss}}$		> 15	> 13 (> 15)		
topness		> 8	< 8		
$\Delta\phi(\text{jet}_i, \vec{p}_{\text{T}}^{\text{miss}})$	[rad]	> 0.9	> 0.6		

selection inverted, and to increase statistics and limit signal contamination, the selection on $\Delta\phi(\text{jet}_i, \vec{p}_{\text{T}}^{\text{miss}})$ is relaxed to 0.6 and the selection on $\Delta\phi(\vec{p}_{\text{T}}^{\text{miss}}, \ell)$ is removed.

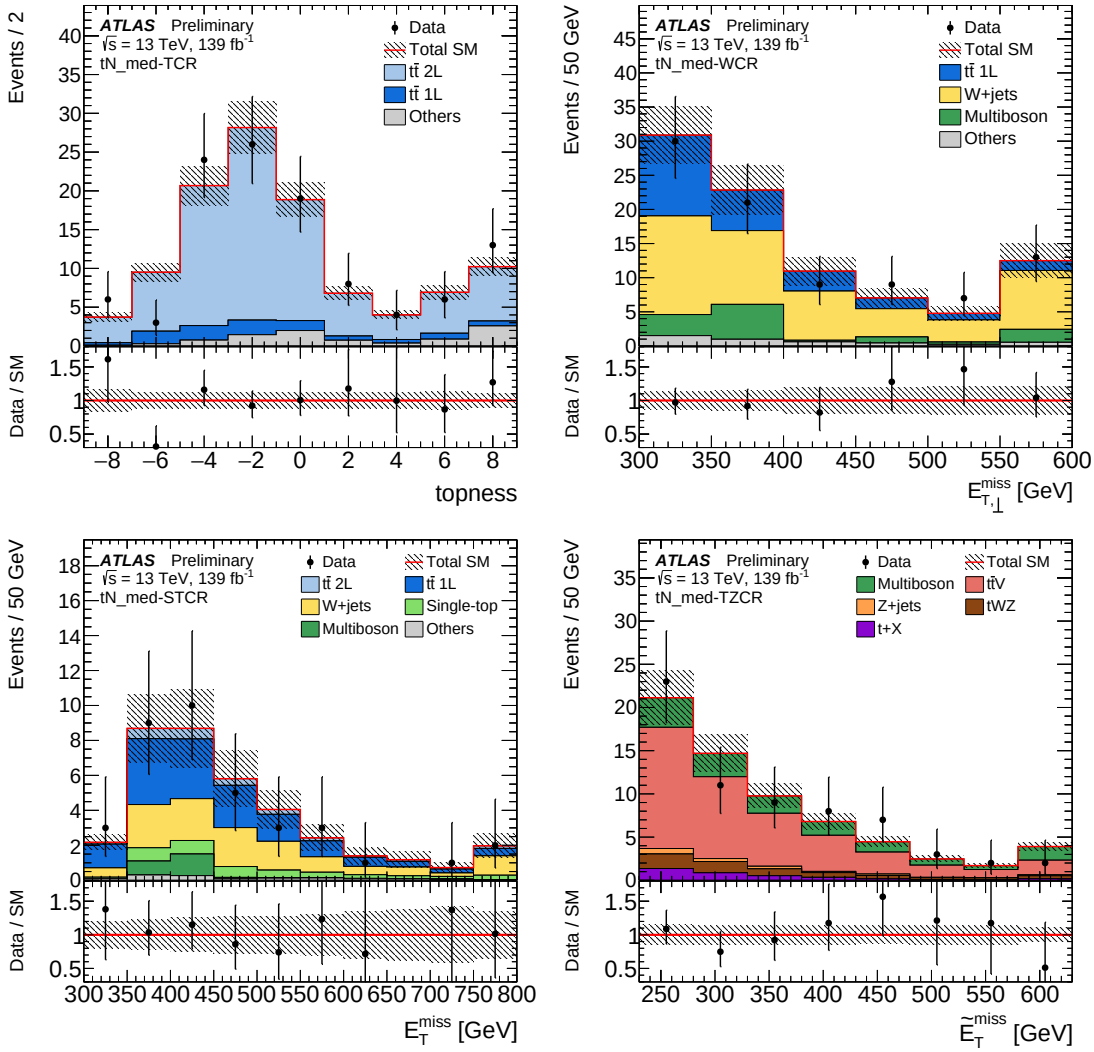

Figure 3: Selected kinematic distributions in `tN_med` CRs: (top left) topness in the TCR, (top right) $E_{\mathrm{T},\perp}^{\mathrm{miss}}$ in the WCR, (bottom left) $E_{\mathrm{T}}^{\mathrm{miss}}$ in the STCR, (bottom right) $\tilde{E}_{\mathrm{T}}^{\mathrm{miss}}$ in the TZCR. The distributions shows are post-fit, meaning that each background is scaled by a normalisation factor obtained from a background-only likelihood fit of the CRs (see Table. 13). The hatched area around the total SM prediction and the hatched band in the Data/SM ratio include all statistical and systematic uncertainties. The last (first) bin contains overflows (underflows).

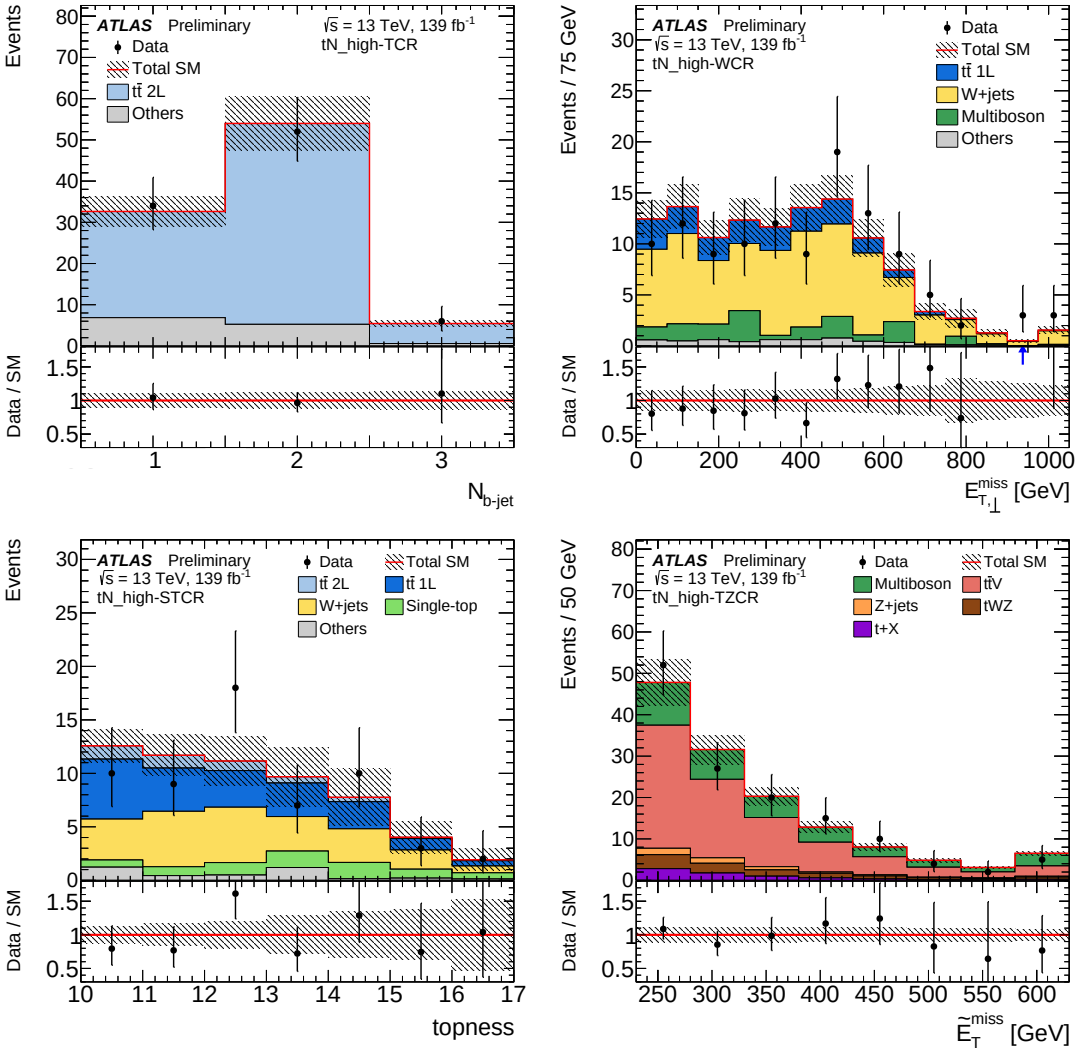

Figure 4: Selected kinematic distributions in `tN_high` CRs: (top left) $N_{b\text{-jet}}$ in the TCR, (top right) $E_{\mathrm{T},\perp}^{\mathrm{miss}}$ in the WCR, (bottom left) topness in the STCR, (bottom right) $\tilde{E}_{\mathrm{T}}^{\mathrm{miss}}$ in the TZCR. The distributions shows are post-fit, meaning that each background is scaled by a normalisation factor obtained from a simultaneous background-only likelihood fit of the CRs (see Table. 13). The hatched area around the total SM prediction and the hatched band in the Data/SM ratio include all statistical and systematic uncertainties. The last (first) bin contains overflows (underflows).

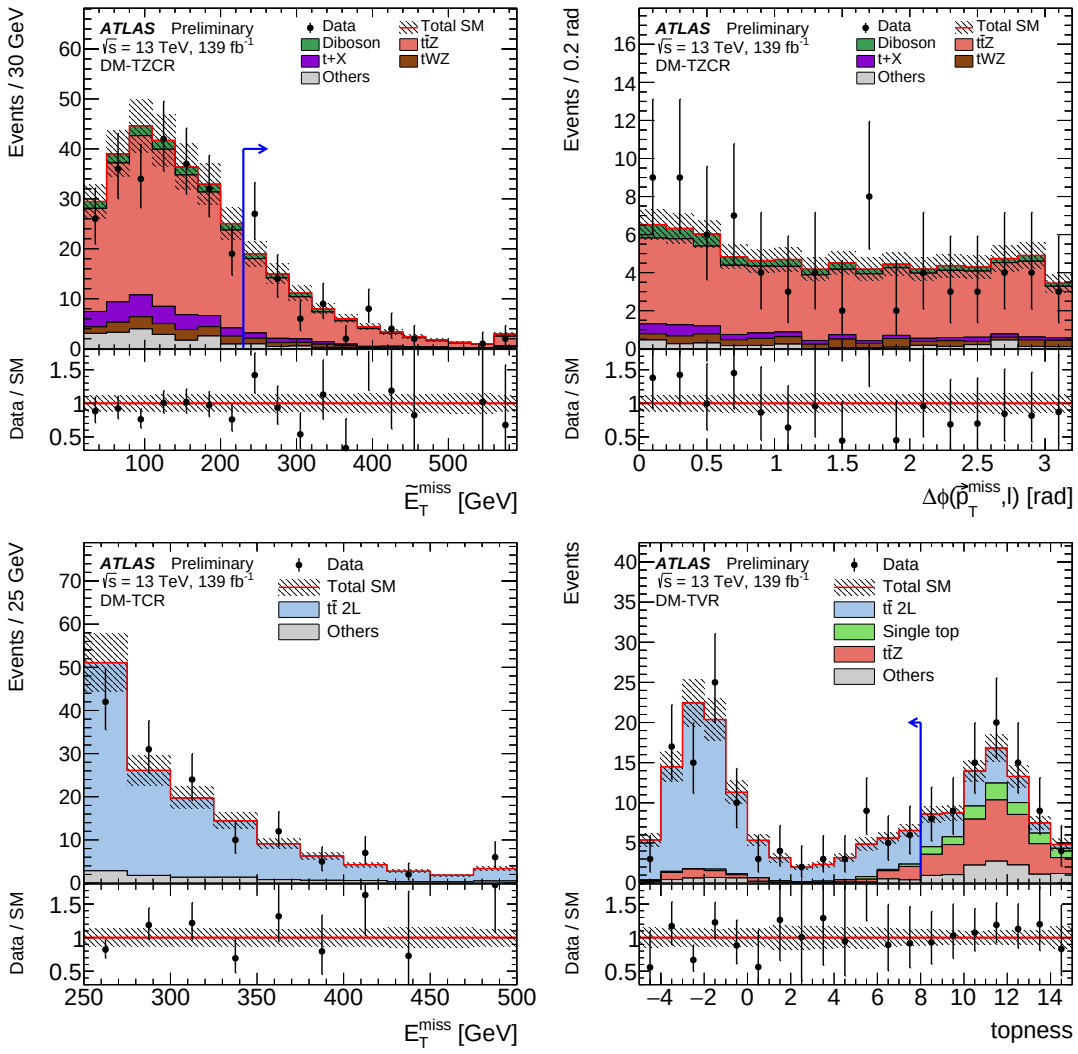

Figure 5: Selected kinematic distributions in DM CRs and VRs: (top left) $\tilde{E}_{\mathrm{T}}^{\mathrm{miss}}$ in the TZCR before applying the $\tilde{E}_{\mathrm{T}}^{\mathrm{miss}}$ selection, (top right) $\Delta\phi(\vec{p}_{\mathrm{T}}^{\mathrm{miss}}, \ell)$ in the TZCR, (bottom left) $E_{\mathrm{T}}^{\mathrm{miss}}$ in the TCR, (bottom right) topness in the TVR before applying the topness selection. For distributions where the requirement on the displayed variable has been removed a blue arrow indicates the final selection on that variable. The distributions shown are post-fit, meaning that each background is scaled by a normalisation factor obtained from a simultaneous background-only likelihood fit of the CRs (see Table. 13). The hatched area around the total SM prediction and the hatched band in the Data/SM ratio include all statistical and systematic uncertainties. The blue arrow shows the last selection that fully defines the region. The last (first) bin contains overflows (underflows).

The tN_med and tN_high definitions permit the construction of a STCR with sufficient data statistics for comparison with the DS- and DR-based Monte Carlo predictions. The STCR is defined with selections close to those of the WCR, but requires a second b-tagged jet, $30 < m_{\mathrm{T}} < 120$ GeV and the distance $\Delta R(b_1, b_2)$ between the two b-tagged jets to be larger than 1.4. To ensure orthogonality with the WCR, events with two b-tagged jets inside the WCR must have $\Delta R(b_1, b_2) < 1.4$. It is found that the DS and DR scheme predictions bracket the observed number of events in the STCR data, with a large discrepancy between the two predictions. The largest discrepancy is observed in the STCR associated with the tN_med SR. The data-to-prediction ratio in the STCR is $0.1^{+0.3}_{-0.1}$ with the DR scheme and 1.5 ± 1.3 with the DS scheme.

The availability of the STCR allows the normalisation of the single-top background to be constrained from data. The fit to the STCR is performed with both DS and DR Monte Carlo schemes, and the resulting two predictions for single-top in the STCR and in the SRs are compatible within uncertainties. Therefore once the STCR is used to constrain the single-top normalisation, the choice of the DS or DR scheme is found to have a negligible impact on the single-top prediction in the SR. In accordance with Ref. [87], the DR scheme is used for the default Wt sample.

Figures 3, 4 and 5 compare data and prediction in CRs and VRs for several variables used in the $\tilde{t}_1 \rightarrow t + \tilde{\chi}_1^0$ and DM SRs. Good agreement is observed between data and prediction, within uncertainties.

8.2 Control and validation regions for compressed $\tilde{t}_1 \rightarrow t + \tilde{\chi}_1^0$

The dominant background processes in both tN_diag_low and tN_diag_high is $t\bar{t}$. Each of these regions has its own dedicated TCR. The TCRs build upon the same N_{jet}, $N_{b\text{-jet}}$, m_{T} and hard-lepton preselection as the SRs. In both TCRs the selection on the p_{T} of the leading jet is lowered compared to the SR, and is selected to be in the range 200−360 GeV for tN_diag_low and in the range 200−440 GeV for tN_diag_high. In the TCR associated to tN_diag_low, $\Delta m_{\mathrm{T}}^{\alpha}$ is required to be below zero to avoid signal contamination. In addition, in order to gain statistics, the selection on $m_{\tilde{t}_1}^{\text{lep}}$ is removed and the selection on m_{T} is lowered to 110 GeV. The TCR associated with tN_diag_high requires $\Delta m_{\mathrm{T}}^{\text{dyn}}$ below 30 GeV to ensure orthogonality with the SR and limit signal contamination. To increase the number of events in the TCR associated to tN_diag_high, the $E_{\mathrm{T}}^{\text{miss}}$ selection is lowered to 350 GeV and selections on $m_{\tilde{\chi}_1^0}^{\text{dyn}}$ and m_{T2} are removed.

The top background normalisation in the 2-body compressed region is validated using one VR for each of the regions tN_diag_low and tN_diag_high. The TVR corresponding to tN_diag_low is identical to the TCR except for the leading jet p_{T}, required to be above 400 GeV. The TVR associated to tN_diag_high is identical to the TCR, but requires the leading jet p_{T} to be larger than 440 GeV. Table 10 summarises the definitions of the TCR and TVR for tN_diag_low and tN_diag_high with respect to the SR definitions.

Figure 6 compares data and prediction in CRs and VRs for several variables used in the tN_diag_low and tN_diag_high SRs. Good agreement is observed between data and prediction, within uncertainties.

Table 10: Event selections defining the tN_diag_low and tN_diag_high TCR and TVR with respect to their respective signal region.

Selection		tN_diag_low	tN_diag_high-TCR	tN_diag_high-TVR
Leading jet p_{T}	[GeV]	>400	[200, 360]	>400
m_{T}	[GeV]	>150	>110	
$\Delta m_{\mathrm{T}}^{\alpha}$	[GeV]	> 40	<0	
$m_{\tilde{t}_1}^{\mathrm{lep}}$	[GeV]	< 600	–	
Selection		tN_diag_high	tN_diag_high-TCR	tN_diag_high-TVR
Leading jet p_{T}	[GeV]	>400	[200, 440]	>440
$E_{\mathrm{T}}^{\mathrm{miss}}$	[GeV]	>400	>350	
m_{T2}	[GeV]	<360	–	
$\Delta m_{\mathrm{T}}^{\mathrm{dyn}}$	[GeV]	>60	<30	
$m_{\tilde{\chi}_1^0}^{\mathrm{dyn}}$	[GeV]	[220, 595]	–	

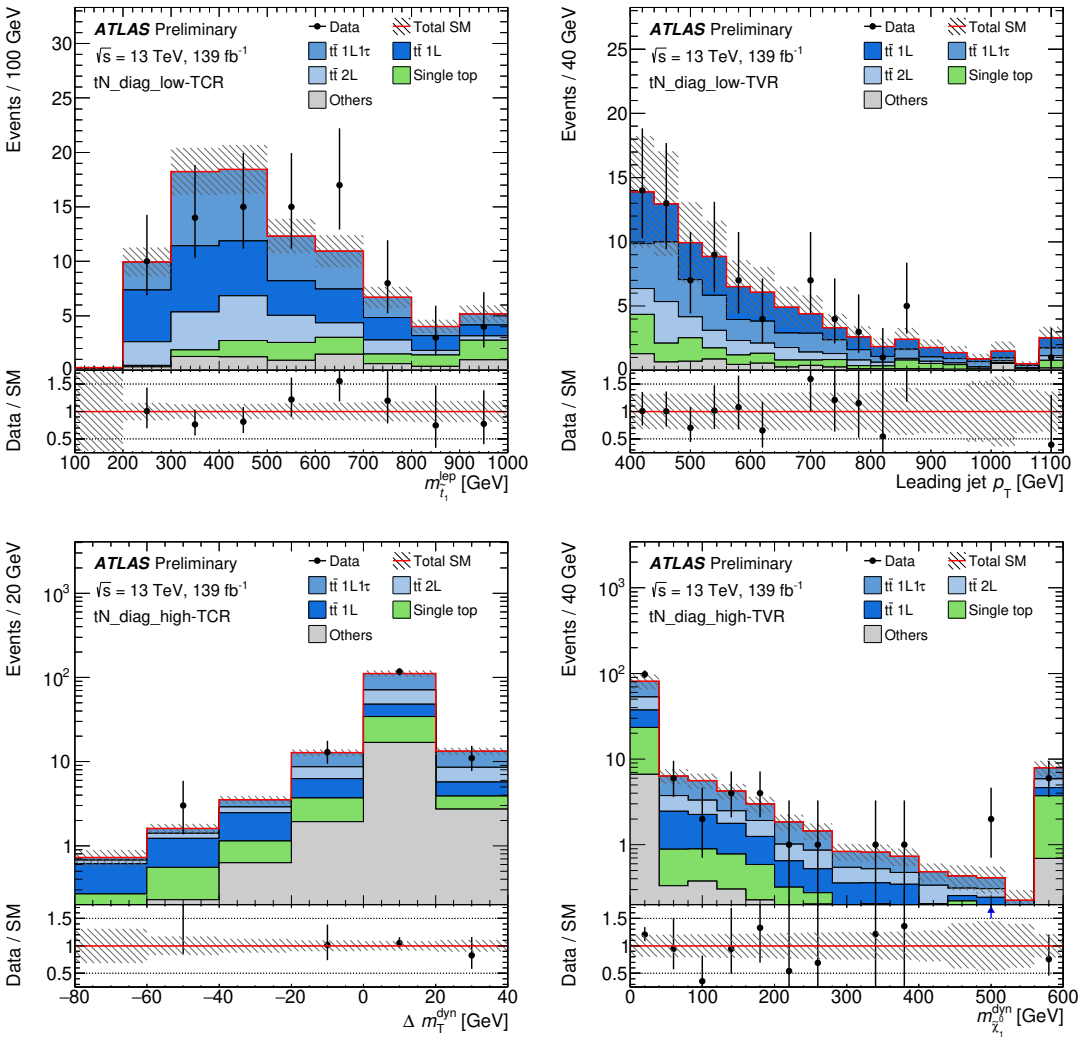

Figure 6: Selected kinematic distributions in `tN_diag_low` and `tN_diag_high` TCRs and TVRs: (top left) $m_{\tilde{t}_1}^{\text{lep}}$ in the `tN_diag_low` TCR, (top right) leading jet p_{T} in the `tN_diag_low` TVR, (bottom left) $\Delta m_{\text{T}}^{\text{dyn}}$ in the `tN_diag_high` TCR, (bottom right) $m_{\tilde{\chi}_1^0}^{\text{dyn}}$ in the `tN_diag_high` TVR. The distributions shown are post-fit, meaning that each background is scaled by a normalisation factor obtained from a simultaneous background-only likelihood fit of the CRs (see Table. 13). The hatched area around the total SM prediction and the hatched band in the Data/SM ratio include all statistical and systematic uncertainties. The last (first) bin contains overflows (underflows).

8.3 Control and validation regions for $\tilde{t}_1 \to bff'\tilde{\chi}_1^0$

In the signal region `bffN_softb` the largest background is W+jets followed by approximately equal amounts of dileptonic and semi-leptonic $t\bar{t}$. A $t\bar{t}$ control region, TCR, is designed to have approximately equal amounts of the two types of $t\bar{t}$ backgrounds. The TCR builds on the same selections as `bffN_softb`, however it requires the presence of at least one b-tagged jet, to increase the fraction of $t\bar{t}$ and to ensure orthogonality with the `bffN_softb` SR. The TCR also requires $p_{\mathrm{T}}^{\ell}/E_{\mathrm{T}}^{\mathrm{miss}}$ to be in the interval [0.12, 0.25] and that the lepton charge be negative. The WCR builds upon the same selections as the SR, but $p_{\mathrm{T}}^{\ell}/E_{\mathrm{T}}^{\mathrm{miss}}$ is required to be in the interval [0.16, 0.32] and the fraction of W+jets events is enhanced by requiring the lepton to be positively charged.

The validation region TVR associated with `bffN_softb` is defined with the same selections as the TCR, except for the ratio $p_{\mathrm{T}}^{\ell}/E_{\mathrm{T}}^{\mathrm{miss}}$ that is required to be in [0.08, 0.12]. The WVR for `bffN_softb` has the same selections at the WCR, however $p_{\mathrm{T}}^{\ell}/E_{\mathrm{T}}^{\mathrm{miss}}$ is required to be in [0.08, 0.16]. Table 11 outlines the differences in selections between the `bffN_softb` SR and the associated CRs and VRs.

The soft b-tagging efficiency and mis-tag rate depend on the track multiplicity, kinematics of the b-hadrons, and the b-hadrons fragmentation. Two high-statistics soft b-tagging regions enriched in $t\bar{t}$ and W+jets are defined, where it is found that the track multiplicity differs between data and Monte Carlo simulations. In each region a weight function with respect to the track multiplicity is defined to reweight the Monte Carlo to the data. After reweighting, a good agreement is found between the data and the simulation in a range of secondary vertex variables such as vertex mass, vertex momentum, vertex distance to the primary vertex and vertex track multiplicity. The ratio of efficiencies and mis-tag rate after-to-before reweighting defines scale factors that are derived separately for Sherpa and Pythia 8. The largest discrepancy after reweighting is found in the W+jets region and is of the order of 20%. A corresponding 20% systematic uncertainty on the soft b-tagging scale factors is introduced.

Table 11: Event selections defining the CRs and VRs in `bffN_softb` and `bffN_btag` relative to their respective signal region.

Selection		`bffN_softb`	`bffN_softb`-TCR (-TVR)	`bffN_softb`-WCR (-WVR)
$N_{b\text{-jet}}$		=0	≥ 1	=0
Lepton charge		–	< 0	> 0
$p_{\mathrm{T}}^{\ell}/E_{\mathrm{T}}^{\mathrm{miss}}$		< 0.04	$\in [0.12, 0.25]$ ($\in [0.08, 0.12]$)	$\in [0.16, 0.32]$ ($\in [0.08, 0.16]$)
Selection		**`bffN_btag`**	**`bffN_btag`-TCR (-TVR)**	**`bffN_btag`-WCR (-WVR)**
b-jet p_{T}	[GeV]	<50	>100 ($\in [50, 100]$)	–
m_{T}	[GeV]	>90	>110	>90
$p_{\mathrm{T}}^{\ell}/E_{\mathrm{T}}^{\mathrm{miss}}$		< 0.05	> 0.05	> 0.05
$\Delta\phi(p_{\mathrm{T}}^{b-\mathrm{jet}}, \vec{p}_{\mathrm{T}}^{\mathrm{miss}})$	[rad]	< 1.5	< 1.5	> 2.3 ($\in [1.5, 2.3]$)
Lepton charge		–	–	>0

In the signal region `bffN_btag`, the dominant background process is dileptonic $t\bar{t}$, representing almost half of all background events, followed by W+jets. In order to ensure orthogonality with the SR and limit signal contamination, the TCR control region has the same selections as the SR, but requires the leading b-tagged jet p_{T} to be above 100 GeV, m_{T} >110 GeV and $p_{\mathrm{T}}^{\ell}/E_{\mathrm{T}}^{\mathrm{miss}}$>0.05. With respect to the SR, the WCR

removes the upper cut on the leading b-tagged jet p_{T}, requires $\Delta\phi(p_{\mathrm{T}}^{b-\mathrm{jet}}, \vec{p}_{\mathrm{T}}^{\mathrm{miss}}) > 2.3$, $p_{\mathrm{T}}^{\ell}/E_{\mathrm{T}}^{\mathrm{miss}}$>0.05 and a positive lepton charge.

The TVR associated to the `bffN_btag` signal region has the same selections as TCR but the b-tagged jet p_{T} must be in the interval [50, 100] GeV, thus between the signal and the control region. The WVR has the same selections at the WCR except for the angle $\Delta\phi(p_{\mathrm{T}}^{b-\mathrm{jet}}, \vec{p}_{\mathrm{T}}^{\mathrm{miss}})$ that is required to be in the intermediate range between WCR and the SR, namely the interval [1.5, 2.3].

Figures 7 and 8 compare data and predictions in the `bffN_softb` and `bffN_btag` CRs and VRs. Good agreement is observed between data and prediction, within uncertainties.

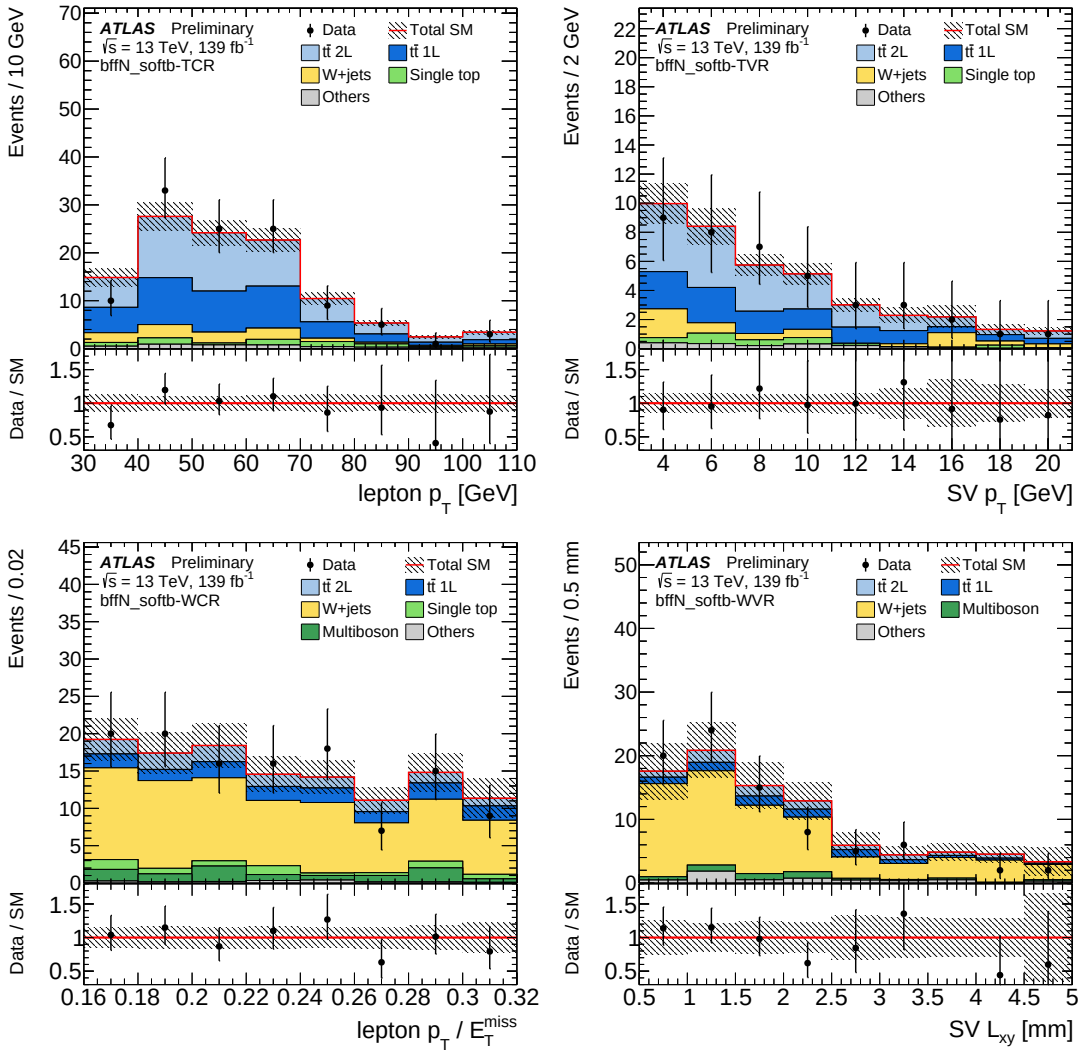

Figure 7: Selected kinematic distributions in `bffN_softb` CRs and VRs: (top left) lepton p_{T} in the TCR, (top right) transverse momentum of the total track momentum attached to the secondary vertex SV p_{T} in the TVR, (bottom left) $p_{\mathrm{T}}^{\ell}/E_{\mathrm{T}}^{\mathrm{miss}}$ in the WCR, (bottom right) distance from the primary vertex to the secondary vertex in the transverse plane SV L_{xy} in the WVR. The distributions shown are post-fit, meaning that each of the backgrounds is scaled by a normalisation factor obtained from a simultaneous background-only likelihood fit of the CRs (see Table. 13). The hatched area around the total SM prediction and the hatched band in the Data/SM ratio include all statistical and systematic uncertainties. The last (first) bin contains overflows (underflows).

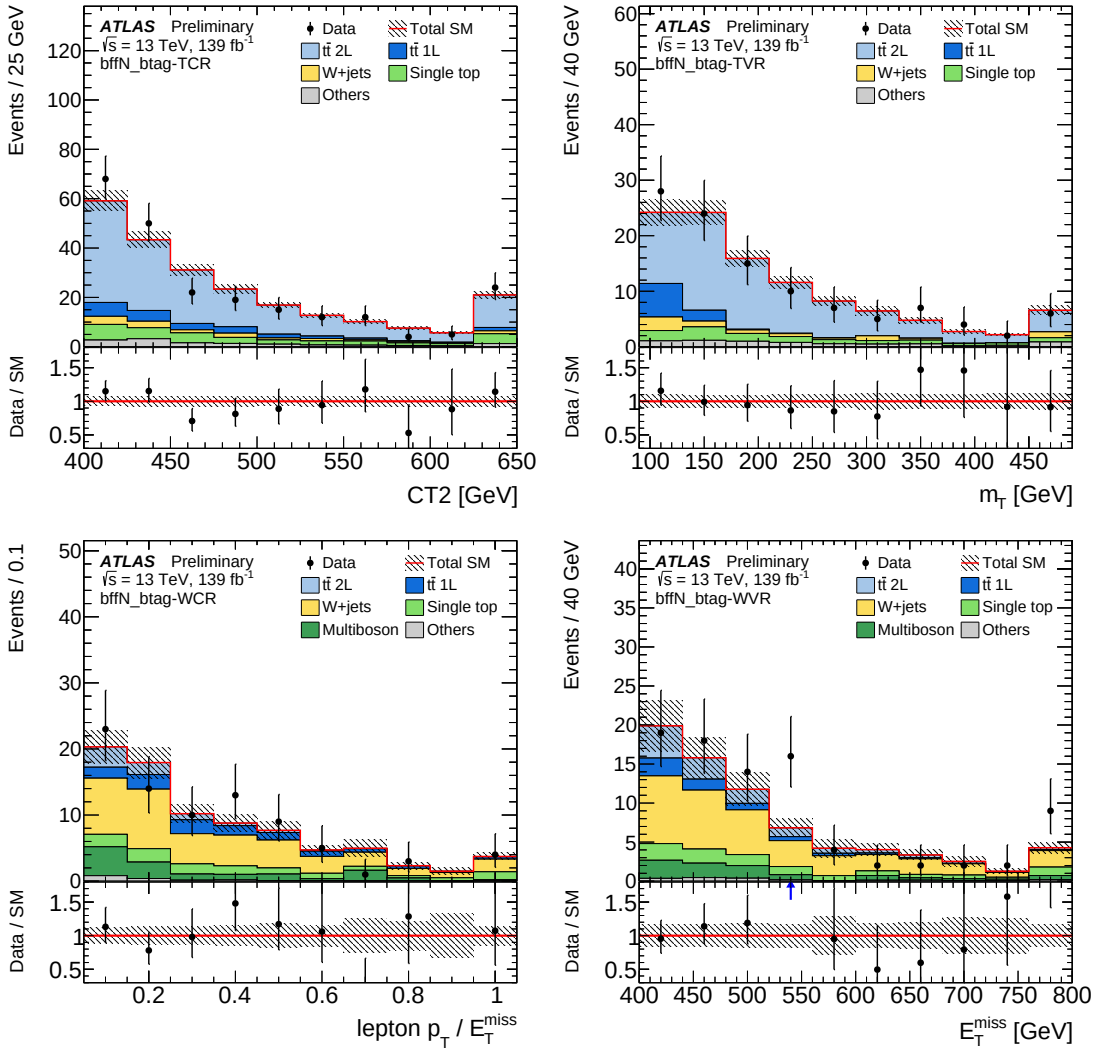

Figure 8: Selected kinematic distributions in `bffN_btag` CRs and VRs: (top left) CT2 in the TCR, (top right) m_{T} in the TVR, (bottom left) $p_{\mathrm{T}}^{\ell}/E_{\mathrm{T}}^{\mathrm{miss}}$ in the WCR, (bottom right) $E_{\mathrm{T}}^{\mathrm{miss}}$ in the WVR. The distributions shown are post-fit, meaning that each of the backgrounds is scaled by a normalisation factor obtained from a simultaneous background-only likelihood fit of the CRs (see Table. 13). The hatched area around the total SM prediction and the hatched band in the Data/SM ratio include all statistical and systematic uncertainties. The last (first) bin contains overflows (underflows).

9 Systematic uncertainties

The systematic uncertainties in the background estimates arise from multiple experimental and theoretical sources and can enter the SR background yield either via direct predictions from theoretical cross-sections or from uncertainties in the extrapolation from CRs to SRs. The sources of systematic uncertainties are grouped into categories whose labels are defined in parentheses in the paragraphs below. Their effect on the background predictions in the SRs is summarised in Table 12. The systematic uncertainties are included as nuisance parameters with Gaussian constraints and profiled in the likelihood fits.

Experimental uncertainties arise from imperfect knowledge of the jet energy scale (*JES*), jet energy resolution (*JER*) [110], scale and resolution of the $E_{\mathrm{T}}^{\mathrm{miss}}$ soft term (E_T^{miss} *experimental*) [120], as well as the modelling of the *b*-tagging or soft *b*-tagging efficiencies and mis-tag rates [114] (*b-tagging experimental*). Other sources of experimental uncertainties arise from the modelling of the lepton energy scales, energy resolutions, reconstruction and identification efficiencies (*Leptons experimental*). There is also an experimental uncertainty arising from the reweighting of the simulation with respect to the number of interactions per bunch crossing in data and the additional cuts applied to jets to ensure they arise from the hard scatter primary vertex (*Pile-up*).

Backgrounds such as diboson and Z+jets, derived directly from a Monte Carlo prediction and a theoretical cross-section, receive theoretical systematic uncertainties (*Theory*) from theoretical cross-section calculations, including those related to parton distribution functions, factorisation and normalisation scales. As shown in Table 8, also the single-top, $t\bar{t}+Z$ and W+jets backgrounds are predicted directly from Monte Carlo simulations for some SRs, in which case the theory uncertainties apply also to those processes.

When the yield from a background such as $t\bar{t}$, single-top, $t\bar{t}+V$ or W+jets is normalised using a CR, modelling uncertainties affect the extrapolation from the control to the signal region, but not the overall normalisation. In each of these cases, the background receives a normalisation systematic uncertainty (*Normalisation*) from the fit, arising from the statistical power of the CR for the given background and a modelling uncertainty (*Modelling*) that affects the extrapolation factor from the CR to the SR.

The uncertainties in the modelling of the $t\bar{t}$ background include effects related to the MC event generator, the hadronisation modelling and the amount of initial and final state radiation [85]. The MC generator uncertainty is estimated by taking the full difference in event yields between Powheg-Box v2+Pythia 8 and MG5_aMC@NLO v2.6.0+Pythia 8. Events generated with Powheg-Box v2 are showered and subsequently hadronised with either Pythia 8 or Herwig 7.0 in order to estimate the effect from modelling of the hadronisation. The systematic uncertainty from the amount of initial and final state radiation is derived by comparing Powheg-Box results obtained with different shower radiation, NLO radiation and modified factorisation and renormalisation scales.

The single-top Wt process modelling uncertainty is derived from the size of the interference between $t\bar{t}$ and Wt. It is obtained by generating separate samples for $t\bar{t}$, Wt and $WWbb$ with MadGraph as LO multi-leg processes and comparing Wt with the difference between $WWbb$ and $t\bar{t}$. The Wt sample generated with MadGraph is found to be in good agreement with the nominal samples generated with Powheg-Box v2+Pythia 8. For the `tN_med` and `tN_high` SRs where STCR is used, the Wt modelling uncertainty enters via the ratio of the number of Wt events in the signal and the STCR. Given the potentially large modelling uncertainty on the interference between $t\bar{t}$ and Wt, the modelling uncertainty is also evaluated for the `DM` SR by comparing the predicted single-top yield from Wt versus the difference between $WWbb$ and $t\bar{t}$.

Table 12: Summary of the dominant systematic uncertainties in % of the total predicted background yields in the SRs, obtained from the background-only fits described in Section 10.

SR Uncertainty (%)	tN_med	tN_high	tN_diag_low	tN_diag_high	bffN_btag	bffN_softb	DM
$t\bar{t}$ normalisation	4.4	2.7	12.3	15.8	6.6	3.7	2.1
$t\bar{t}+Z$ normalisation	9.0	6.8	–	–	–	–	8.0
W+jets normalisation	3.0	4.8	–	–	5.5	11.1	–
Wt normalisation	2.8	3.4	–	–	–	–	–
$t\bar{t}$ modelling	3.0	9.1	18.4	29.3	3.1	3.3	6.1
$t\bar{t}+Z$ modelling	7.7	7.1	–	–	–	–	3.3
W+jets modelling	2.3	3.8	–	–	4.3	9.7	–
Wt modelling	0.5	0.8	–	–	–	–	4.2
JER	10.9	5.1	4.1	5.0	1.8	7.6	8.3
$E_{\mathrm{T}}^{\mathrm{miss}}$ experimental	0.7	0.4	1.0	0.2	2.4	3.4	1.9
b-tagging experimental	1.7	3.6	1.3	0.9	1.9	3.2	4.2
JES	6.0	2.5	4.7	4.1	6.1	11.7	2.5
Leptons experimental	1.0	1.6	1.3	0.3	2.3	4.9	1.2
Pile-up	1.1	1.2	1.2	0.3	1.0	2.1	1.4
Theory	0.9	1.3	1.4	0.5	3.8	3.7	1.1
Monte Carlo statistics	4.1	6.6	5.8	3.5	4.9	17.2	3.2
Total	19	17	24	33	20	27	23

The modelling uncertainties considered for $t\bar{t}+Z$ are the renormalisation and factorisation scales, and the amount of initial and final state radiation, obtained by considering the variation of the same parameters used for the $t\bar{t}$ initial and final state radiation systematics. The W+jets modelling uncertainties include generator modelling, derived by considering an alternative W+jets samples generated with MadGraph as well as modified factorisation, renormalisation, resummation and parton matching scales.

Most of the SRs are binned in one or two variables in order to enhance sensitivity to a wider range of models for exclusion limits. In this situation the normalisation factors to go from the CR to the SR is rederived specifically for each bin of the SR. The modelling systematics are also rederived following the scheme above but applied to the normalisation factor from the CR to each specific bin of the SR.

The SUSY signal cross-section uncertainty is taken from an envelope of cross-section predictions using different PDF sets and factorisation and renormalisation scales as described in Ref. [127]. The uncertainty in the DM production cross-section is derived from the scale variations and PDF choices. Dedicated uncertainties in the SUSY and DM signal acceptance due to the modelling of additional radiation, factorisation, renormalisation and parton matching scales are considered. The total systematic uncertainty for the SUSY models varies between 9% and 35% growing at higher stop mass and at lower values of $\Delta m_{\tilde{t}_1,\tilde{\chi}_1^0}$. For the spin-0 mediator signals the total systematic uncertainty is between 15 and 18%.

10 Results

In order to determine the SM background yields in the SRs, a background-only likelihood fit is performed for each analysis. The fit does not use the signal region data, but only the dedicated CRs to normalise the backgrounds.

The number of observed events and the predicted number of SM background events from the background-only fits in all VRs and SRs are shown in Figure 9 together with the Z significance [128] of the observation[5]. The SRs are not mutually exclusive and are therefore not statistically independent. In all SRs, the distributions indicate good agreement between the data and the SM background estimate. The largest excess over the background-only hypothesis is 1.9σ observed in the `tN_high` SR.

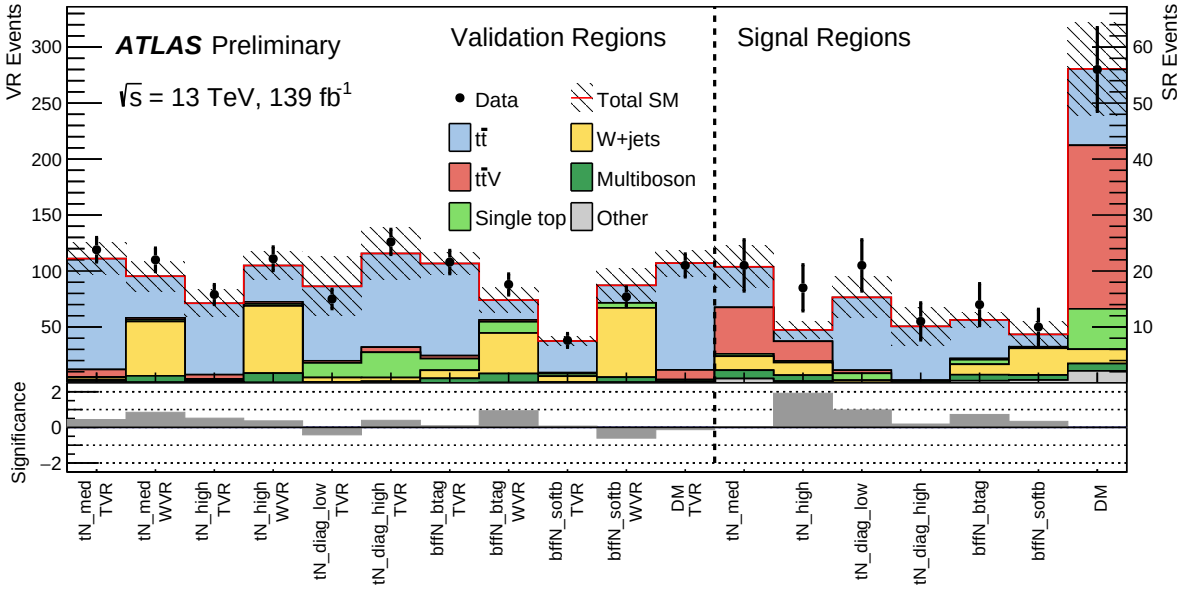

Figure 9: The upper panel shows the comparison between the observed data (n_{obs}) and the predicted SM background (n_{exp}) in all VRs and SRs. The background predictions are obtained using the background-only fit configuration, and the hatched area around the SM prediction includes all uncertainties. The bottom panel shows the Z significance of the observed number of events given the SM expectation.

The number of observed events together with the predicted number of SM background events in all SRs are summarised in Table 13, showing the breakdown of the various backgrounds that contribute to the SRs. The tables also list the results for the fit parameters that control the normalisation of the main backgrounds (normalisation factors, NFs)[6], together with the associated fit uncertainties including the theoretical modelling uncertainties. In order to quantify the level of agreement of the SM background-only hypothesis with the observations in the SRs, a profile-likelihood-ratio test is performed. The resulting

[5] Significance Z of observing n events for a prediction of $b \pm \sigma$ is defined as

$Z = \sqrt{2(n \ln[\frac{n(b+\sigma^2)}{b^2+n\sigma^2}] - \frac{b^2}{\sigma^2} \ln[1 + \frac{\sigma^2(n-b)}{b(b+\sigma^2)}])}$ when $n \geq b$, or

$Z = -\sqrt{2(n \ln[\frac{n(b+\sigma^2)}{b^2+n\sigma^2}] - \frac{b^2}{\sigma^2} \ln[1 + \frac{\sigma^2(n-b)}{b(b+\sigma^2)}])}$ when $n < b$.

[6] The $t\bar{t}$ NFs in the `tN_diag_low`, `bffN_btag`, and `bffN_softb` SRs are applied to both semi-leptonic and dileptonic $t\bar{t}$ events while all other SRs apply the $t\bar{t}$ NFs to the dileptonic component only.

Table 13: The number of observed events in the various SRs together with the expected numbers of background events and their uncertainties as predicted by the background-only fits, the normalisation factors for the background predictions obtained in the fit, the probabilities (represented by p_0 and Z values) that the observed numbers of events are compatible with the background-only hypothesis, and the expected ($N^{\text{limit}}_{\text{non-SM}}$ exp.) and observed ($N^{\text{limit}}_{\text{non-SM}}$ obs.) 95% CL upper limits on the number of beyond-SM events.

	tN_med	tN_high	tN_diag_low	tN_diag_high	bffN_btag	bffN_softb	DM
Observed	21	17	21	11	14	10	56
Total SM	21 ± 4	9.5 ± 1.6	15 ± 4	10.1 ± 3.4	11.3 ± 1.4	8.7 ± 2.3	56 ± 8
$t\bar{t}$	7.2 ± 1.2	2.0 ± 1.0	13.0 ± 2.8	9.6 ± 2.6	6.9 ± 1.1	2.2 ± 0.6	14 ± 4
$t\bar{t}V$	8.3 ± 2.5	3.5 ± 1.0	0.55 ± 0.17	0.12 ± 0.04	0.21 ± 0.12	0.06 ± 0.04	29 ± 6
Single-top	$0.4^{+0.6}_{-0.4}$	$0.27^{+0.34}_{-0.27}$	1.24 ± 0.27	0.26 ± 0.06	0.8 ± 0.5	0.22 ± 0.08	7 ± 4
W+jets	2.5 ± 2.3	2.3 ± 1.0	0.41 ± 0.13	0.080 ± 0.020	1.9 ± 0.8	4.8 ± 2.1	2.56 ± 0.24
Multiboson	1.49 ± 0.21	1.06 ± 0.16	0.070 ± 0.020	0.020 ± 0.010	1.07 ± 0.35	0.89 ± 0.32	1.31 ± 0.18
Other	0.31 ± 0.05	0.160 ± 0.022	-	-	0.40 ± 0.13	0.52 ± 0.19	2.15 ± 0.16
$t\bar{t}$ NF	$0.98^{+0.14}_{-0.12}$	0.90 ± 0.12	$0.88^{+0.13}_{-0.12}$	$0.73^{+0.14}_{-0.13}$	$0.80^{+0.09}_{-0.08}$	0.68 ± 0.10	$1.12^{+0.15}_{-0.13}$
$t\bar{t}V$ NF	$0.95^{+0.22}_{-0.20}$	0.92 ± 0.17	-	-	-	-	$1.18^{+0.20}_{-0.18}$
Single-top NF	$0.11^{+0.26}_{-0.11}$	$0.12^{+0.22}_{-0.12}$	-	-	-	-	-
W+jets NF	$0.96^{+0.25}_{-0.23}$	0.86 ± 0.17	-	-	0.83 ± 0.28	$1.04^{+0.22}_{-0.20}$	-
p_0 (Z)	0.49 (0.03)	0.01 (2.20)	0.17 (0.95)	0.31 (0.50)	0.20 (0.84)	0.26 (0.64)	0.50 (0.00)
$N^{\text{limit}}_{\text{non-SM}}$ exp.	$12.4^{+5.4}_{-2.6}$	$9.8^{+2.8}_{-1.8}$	$14.1^{+4.8}_{-3.3}$	$9.7^{+3.7}_{-2.1}$	$8.6^{+3.6}_{-1.2}$	$8.9^{+3.8}_{-2.0}$	$27.4^{+7.6}_{-5.0}$
$N^{\text{limit}}_{\text{non-SM}}$ obs.	12.9	16.2	17.7	10.9	11.7	10.5	28.2

p-values (p_0) are also presented in the table together with the Z significances. For SRs with an observed number of events below the SM prediction, the p_0 values are capped at 0.5. Model-independent upper limits on beyond-SM contributions are derived for each SR. A generic signal model is assumed that contributes only to the SR and for which neither experimental nor theoretical systematic uncertainties except for the luminosity uncertainty are considered. All limits are calculated using the CL_s prescription [129]. The NFs are compatible with unity in most cases. One exception is for the single-top NFs in the `tN_med` and `tN_high` SRs. The single-top NFs are significantly below unity when using the DR scheme for the treatment of the interference between the Wt and $t\bar{t}$ processes. When changing to the DS scheme, the NFs become larger than unity but the predicted number of single-top events in the signal regions after the fit does not change significantly. The $t\bar{t}$ NFs in `tN_diag_high` `bffN_btag` and `bffN_softb` are below unity. This is due to the imperfect modeling of the high-p_{T} ISR jet required for triggering.

Figures 10 and 11 show comparisons between the observed data and the SM background prediction with all SR selections applied except the requirement on the plotted variable. The expected distributions from representative signal benchmark models are overlaid.

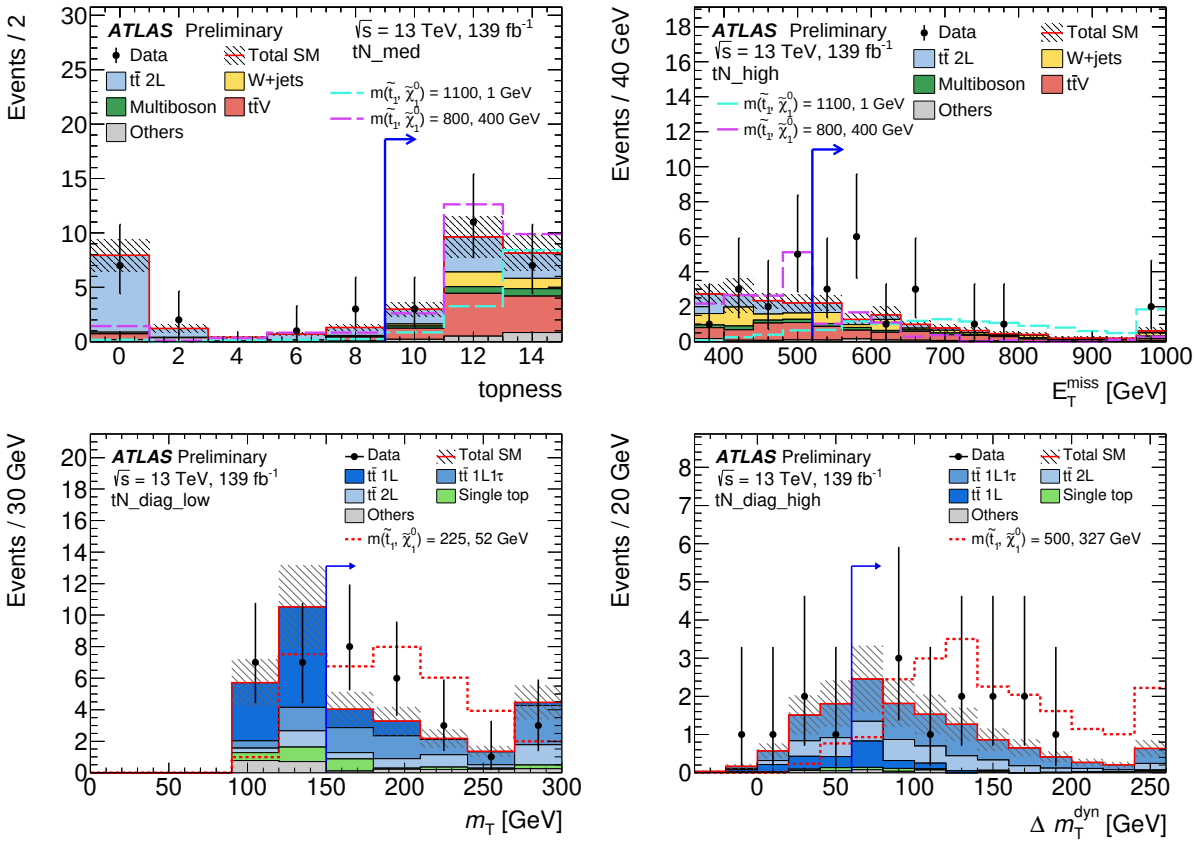

Figure 10: Kinematic distributions in the `tN_med` (top left), `tN_high` (top right), `tN_diag_low` (bottom left), `tN_diag_high` (bottom right) SRs. The full event selection in the corresponding signal region is applied, except for the requirement (indicated by an arrow) that is imposed on the variable being plotted. The distributions shown are post-fit, meaning that the predicted SM backgrounds are scaled with the normalisation factors obtained from the corresponding control regions in Table 13. In addition to the background prediction, a signal model is shown on each plot. The hatched area around the total SM prediction includes statistical and experimental uncertainties. The last (first) bin contains overflows (underflows).

11 Interpretations

No significant excess is observed, and exclusion limits are set based on profile-likelihood fits for the stop pair production models and the spin-0 mediator models. Exclusion limits at 95% confidence level (CL) are obtained by selecting the signal region with the lowest expected CL_s value for each signal model and the exclusion contours are derived by interpolating in the CL_s value. The signal uncertainties and potential signal contributions to all regions are taken into account, and all uncertainties except those in the theoretical signal cross-section are included in the fit. In all exclusion plots, the $\pm 1\sigma_{\text{exp}}$ uncertainty band indicates how much the expected limit is affected by the systematic and statistical uncertainties included in the fit. The $\pm 1\sigma^{\text{SUSY}}_{\text{theory}}$ uncertainty lines around the observed limit illustrate the change in the observed limit as the nominal signal cross-section is scaled up and down by the theoretical cross-section uncertainty.

Figures 12 and 13 show the expected and observed exclusion contours as a function of the stop mass, the neutralino mass and the mass difference between the stop and the neutralino, for the $\tilde{t}_1 \rightarrow t + \tilde{\chi}^0_1$,

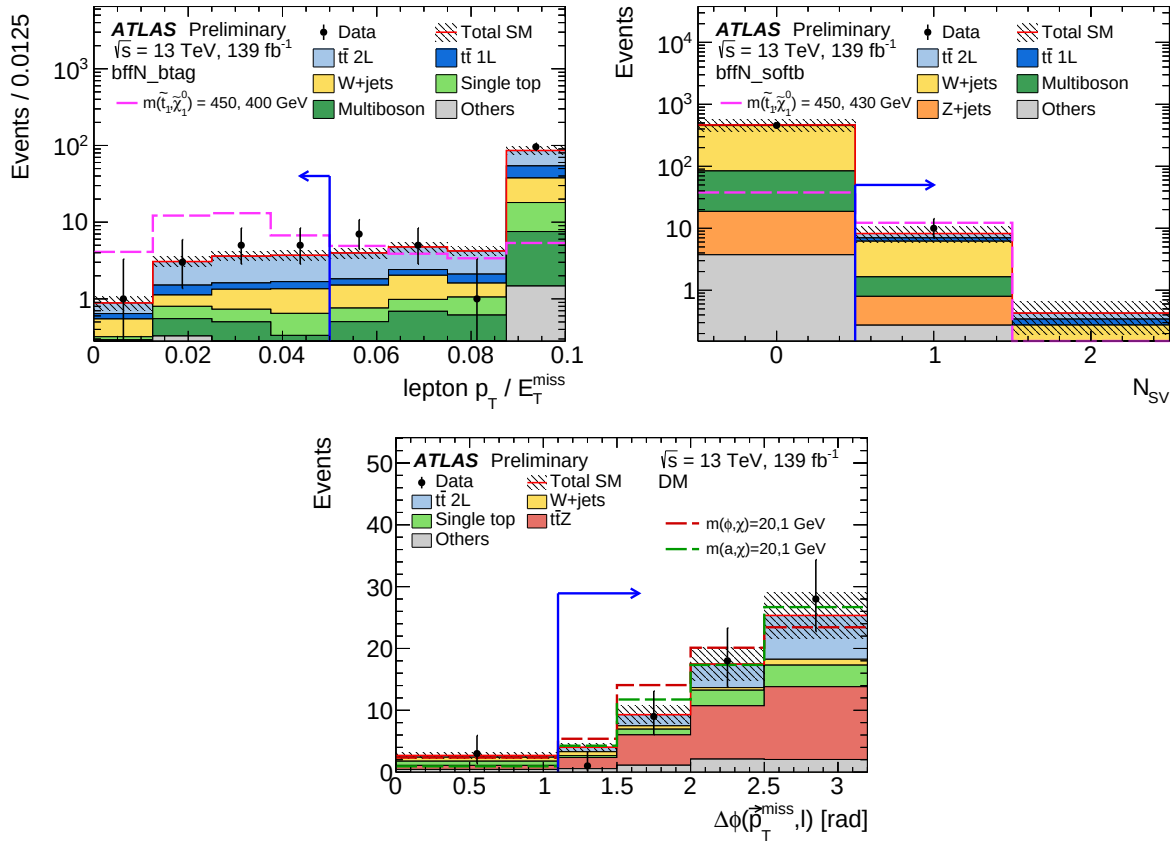

Figure 11: Kinematic distributions in the `bffN_btag` (top left), `bffN_softb` (top right), and `DM` (bottom right) SRs. The full event selection in the corresponding signal region is applied, except for the requirement (indicated by an arrow) that is imposed on the variable being plotted. The distributions shown are post-fit, meaning that the predicted SM backgrounds are scaled with the normalisation factors obtained from the corresponding control regions in Table 13. In addition to the background prediction, a signal model is shown on each plot. The hatched area around the total SM prediction includes statistical and experimental uncertainties. The last (first) bin contains overflows (underflows).

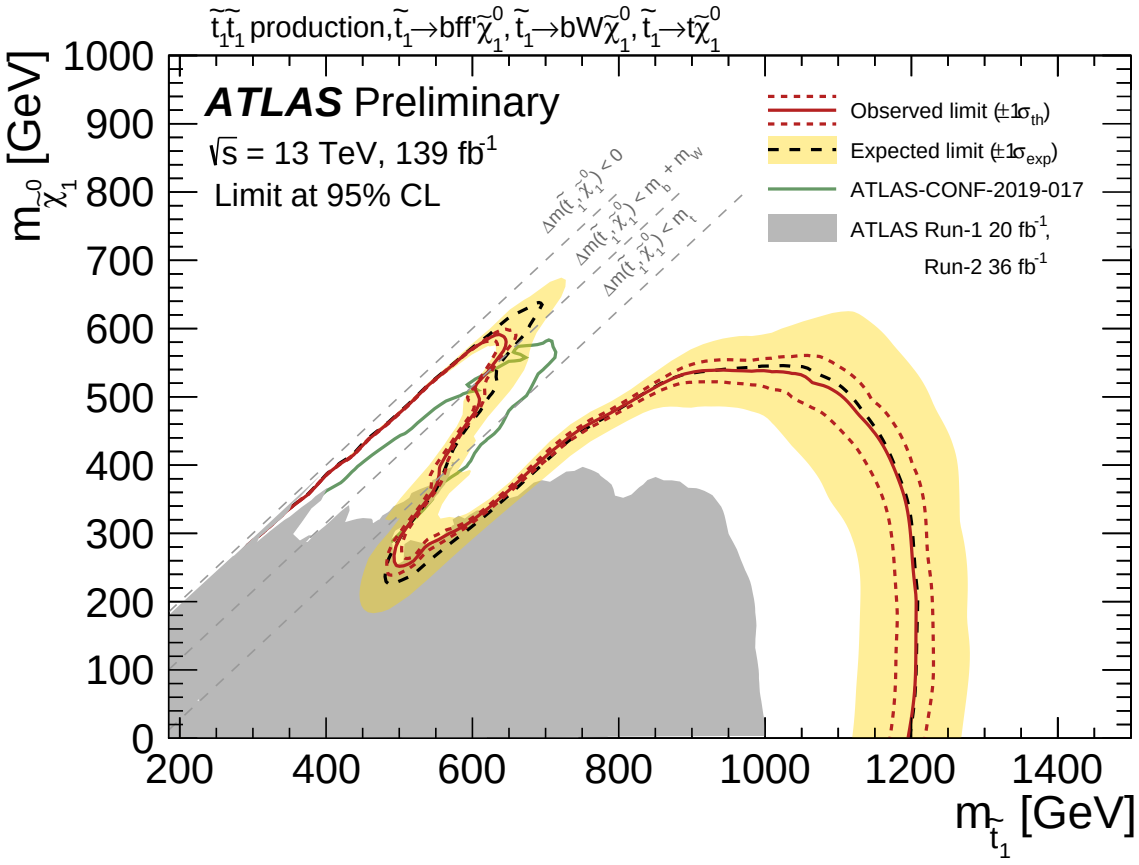

Figure 12: Expected (black dashed) and observed (red solid) 95% excluded regions in the plane of $m_{\tilde{\chi}_1^0}$ and $m_{\tilde{t}_1}$ for direct stop pair production assuming either a $\tilde{t}_1 \to t + \tilde{\chi}_1^0$, $\tilde{t}_1 \to bW\tilde{\chi}_1^0$ or $\tilde{t}_1 \to bff'\tilde{\chi}_1^0$ decay with a branching ratio of 100%. The excluded regions from previous publications [27–29] are shown with the grey shaded area and the green line [45], with the latter being the preliminary result on the full Run 2 data set assuming a $\tilde{t}_1 \to bW\tilde{\chi}_1^0$ decay. The dashed grey lines indicate the kinematical border of the stop decay.

$\tilde{t}_1 \to bW\tilde{\chi}_1^0$ and $\tilde{t}_1 \to bff'\tilde{\chi}_1^0$ scenarios. The exclusion contour obtained by the analysis optimised for the $\tilde{t}_1 \to bW\tilde{\chi}_1^0$ is superimposed [45]. In models with a massless neutralino, stop masses up to 1200 GeV are excluded at 95% CL. In the diagonal region, where the mass difference between the stop and the neutralino coincides with the mass of the top quark, stop masses up to 570 GeV are excluded. In the four-body region, stop masses up to 640 GeV are excluded for a neutralino mass of approximately 580 GeV. The small excess observed in `tN_high` is not visible in the exclusion limits as the shape fit used to obtain exclusion results is based on the `tN_med` selection criteria (see Table 4). In particular the $E_{\mathrm{T},\perp}^{\mathrm{miss}}$ requirement applied in `tN_med` but not in `tN_high` removes much of the excess. The shape fit has better expected sensitivity than the single-bin SRs over the whole $\tilde{t}_1 \to t + \tilde{\chi}_1^0$ parameter space.

Figure 14 shows the upper limit on the ratio of the production cross-section for the spin-0 mediator model to the theoretical cross-section. Limits are shown under the hypothesis of a scalar or pseudo-scalar mediator for a fixed DM candidate mass. Scalar and pseudo-scalar mediator masses up to approximately 200 GeV are excluded at 95% CL, assuming a 1 GeV dark matter particle mass and a common coupling of $g = 1$ to SM and dark matter particles. With the common coupling reduced to $g = 0.8$, mediator masses up to approximately 100 GeV are excluded. Models with a mediator mass of 10 GeV and a dark matter particle

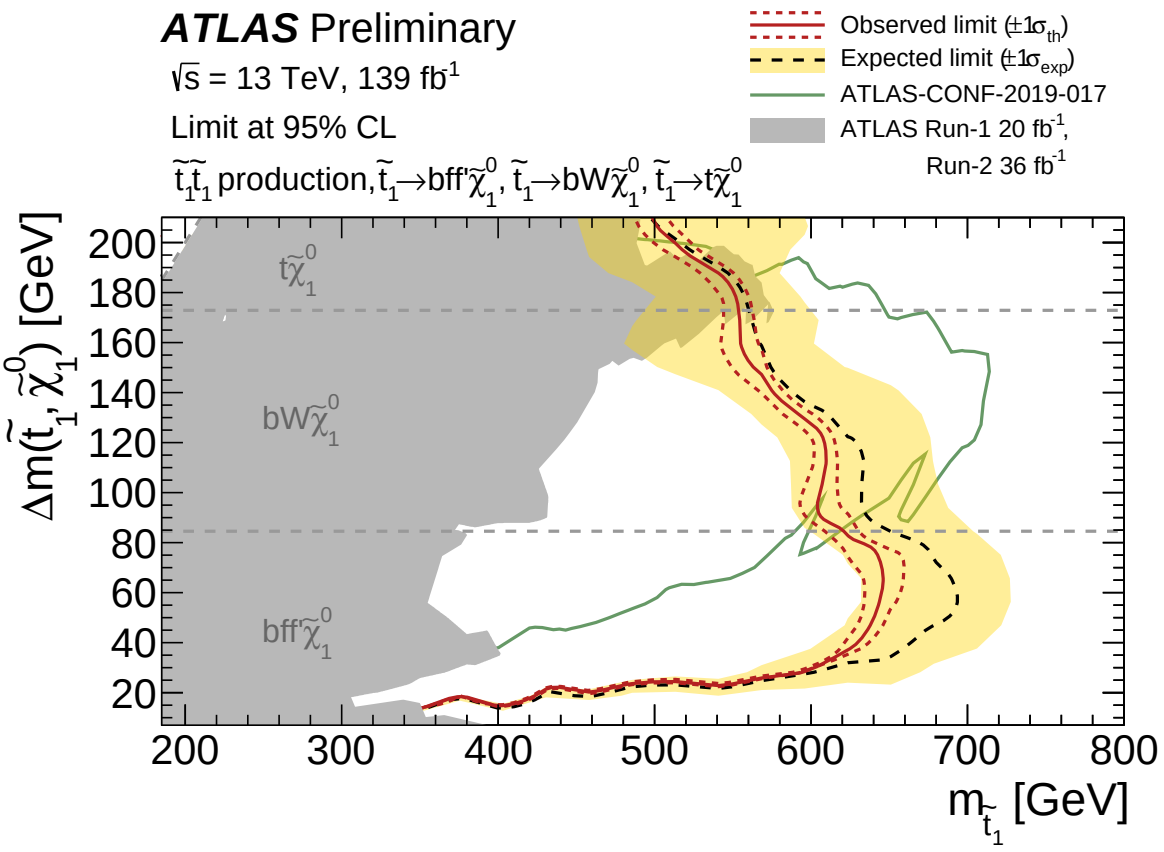

Figure 13: Expected (black dashed) and observed (red solid) 95% excluded regions in the plane of $\Delta(m_{\tilde{t}_1}, m_{\tilde{\chi}_1^0})$ and $m_{\tilde{t}_1}$ for direct stop pair production assuming either a $\tilde{t}_1 \to t + \tilde{\chi}_1^0$, $\tilde{t}_1 \to bW\tilde{\chi}_1^0$ or $\tilde{t}_1 \to bff'\tilde{\chi}_1^0$ decay with a branching ratio of 100%. The excluded regions from previous publications [27–29] are shown with the grey shaded area and the green line [45], with the latter being the preliminary result on the full Run 2 data set assuming a $\tilde{t}_1 \to bW\tilde{\chi}_1^0$ decay. The dashed grey lines indicate the kinematical border of the stop decay.

mass of 1 GeV are excluded down to a coupling of approximately $g = 0.7$.

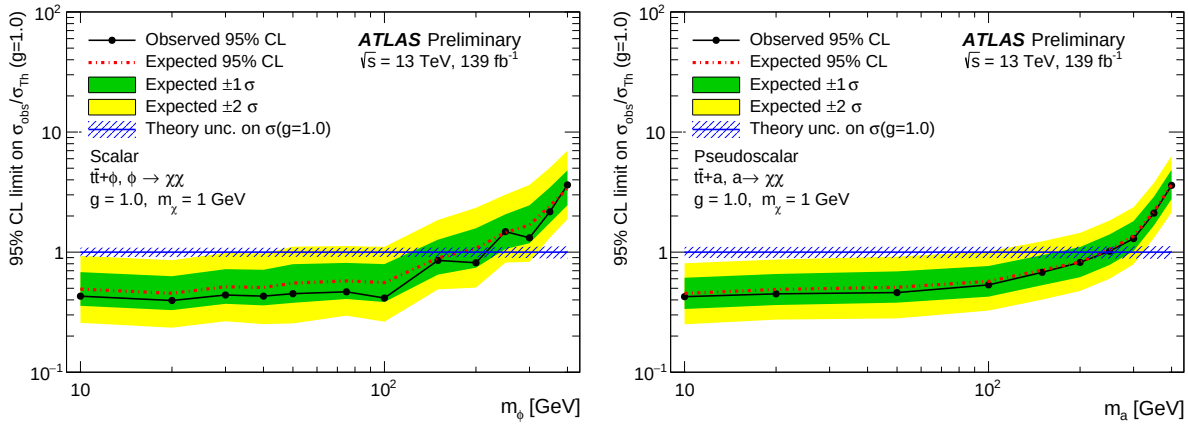

Figure 14: Upper limit on the ratio of the production cross-section for the spin-0 mediator model to the theoretical cross-section under the hypothesis of (left) a scalar or (right) a pseudo-scalar mediator. The limit is shown as a function of the mediator mass for a fixed mass of the DM candidate of 1 GeV. The coupling of the mediator to SM and DM particles is assumed to be $g = 1$.

12 Conclusion

This paper presents searches for direct stop pair production covering various SUSY phase space and searches for a spin-0 mediator decaying into pair-produced dark-matter particles. The searches use the final state with one isolated lepton, jets, and $E_{\mathrm{T}}^{\mathrm{miss}}$.

The searches use 139 fb^{-1} of pp collision data collected by the ATLAS experiment at the LHC at a centre-of-mass energy of $\sqrt{s} = 13$ TeV. The largest excess over the background-only hypothesis is 1.9σ in the `tN_high` SR. As no significant deviation from the Standard Model expectation is observed, exclusion limits at 95% confidence level are derived for the considered models. Stops are excluded up to 1200 GeV in the two-body decay scenario. In the four-body scenario stops up to 640 GeV are excluded for a stop–neutralino mass difference of 60 GeV. Scalar and pseudoscalar dark-matter mediators are excluded up to 200 GeV for a common coupling of $g = 1$ to SM and dark-matter particles.

References

[1] Y. A. Golfand and E. P. Likhtman,
Extension of the Algebra of Poincare Group Generators and Violation of p Invariance,
JETP Lett. **13** (1971) 323, [Pisma Zh. Eksp. Teor. Fiz. 13 (1971) 452].

[2] D. V. Volkov and V. P. Akulov, *Is the Neutrino a Goldstone Particle?*, Phys. Lett. B **46** (1973) 109.

[3] J. Wess and B. Zumino, *Supergauge Transformations in Four-Dimensions*,
Nucl. Phys. B **70** (1974) 39.

[4] J. Wess and B. Zumino, *Supergauge Invariant Extension of Quantum Electrodynamics*,
Nucl. Phys. B **78** (1974) 1.

[5] S. Ferrara and B. Zumino, *Supergauge Invariant Yang-Mills Theories*,
Nucl. Phys. B **79** (1974) 413.

[6] A. Salam and J. A. Strathdee, *Supersymmetry and Nonabelian Gauges*,
Phys. Lett. B **51** (1974) 353.

[7] G. R. Farrar and P. Fayet, *Phenomenology of the Production, Decay, and Detection of New Hadronic States Associated with Supersymmetry*, Phys. Lett. B **76** (1978) 575.

[8] ATLAS Collaboration, *Observation of a new particle in the search for the Standard Model Higgs boson with the ATLAS detector at the LHC*, Phys. Lett. B **716** (2012) 1,
arXiv: 1207.7214 [hep-ex].

[9] CMS Collaboration,
Observation of a new boson at a mass of 125 GeV with the CMS experiment at the LHC,
Phys. Lett. B **716** (2012) 30, arXiv: 1207.7235 [hep-ex].

[10] S. Dimopoulos and H. Georgi, *Softly Broken Supersymmetry and SU(5)*,
Nucl. Phys. B **193** (1981) 150.

[11] E. Witten, *Dynamical Breaking of Supersymmetry*, Nucl. Phys. B **188** (1981) 513.

[12] M. Dine, W. Fischler and M. Srednicki, *Supersymmetric Technicolor*,
Nucl. Phys. B **189** (1981) 575.

[13] S. Dimopoulos and S. Raby, *Supercolor*, Nucl. Phys. B **192** (1981) 353.

[14] N. Sakai, *Naturalness in Supersymmetric Guts*, Z. Phys. C **11** (1981) 153.

[15] R. Kaul and P. Majumdar, *Cancellation of Quadratically Divergent Mass Corrections in Globally Supersymmetric Spontaneously Broken Gauge Theories*, Nucl. Phys. B **199** (1982) 36.

[16] R. Barbieri and G. F. Giudice, *Upper Bounds on Supersymmetric Particle Masses*, Nucl. Phys. B **306** (1988) 63.

[17] B. de Carlos and J. A. Casas, *One loop analysis of the electroweak breaking in supersymmetric models and the fine tuning problem*, Phys. Lett. B **309** (1993) 320, arXiv: hep-ph/9303291.

[18] S. Weinberg, *Implications of Dynamical Symmetry Breaking*, Phys. Rev. D **13** (1976) 974.

[19] E. Gildener, *Gauge Symmetry Hierarchies*, Phys. Rev. D **14** (1976) 1667.

[20] S. Weinberg, *Implications of Dynamical Symmetry Breaking: An Addendum*, Phys. Rev. D **19** (1979) 1277.

[21] L. Susskind, *Dynamics of Spontaneous Symmetry Breaking in the Weinberg-Salam Theory*, Phys. Rev. D **20** (1979) 2619.

[22] P. Fayet, *Supersymmetry and Weak, Electromagnetic and Strong Interactions*, Phys. Lett. B **64** (1976) 159.

[23] P. Fayet, *Spontaneously Broken Supersymmetric Theories of Weak, Electromagnetic and Strong Interactions*, Phys. Lett. B **69** (1977) 489.

[24] P. Fayet, *Relations Between the Masses of the Superpartners of Leptons and Quarks, the Goldstino Couplings and the Neutral Currents*, Phys. Lett. B **84** (1979) 416.

[25] H. Goldberg, *Constraint on the Photino Mass from Cosmology*, Phys. Rev. Lett. **50** (1983) 1419, Erratum: Phys. Rev. Lett. 103 (2009) 099905.

[26] J. R. Ellis, J. S. Hagelin, D. V. Nanopoulos, K. A. Olive and M. Srednicki, *Supersymmetric Relics from the Big Bang*, Nucl. Phys. B **238** (1984) 453.

[27] ATLAS Collaboration, *Search for top squark pair production in final states with one lepton, jets, and missing transverse momentum using* 36 fb^{-1} *of* $\sqrt{s}$ = 13 *TeV pp collision data with the ATLAS detector*, JHEP **06** (2018) 108, arXiv: 1711.11520 [hep-ex].

[28] ATLAS Collaboration, *Search for a scalar partner of the top quark in the jets plus missing transverse momentum final state at* $\sqrt{s}$ = 13 *TeV with the ATLAS detector*, JHEP **12** (2017) 085, arXiv: 1709.04183 [hep-ex].

[29] ATLAS Collaboration, *Search for direct top squark pair production in final states with two leptons in* $\sqrt{s}$ = 13 *TeV pp collisions with the ATLAS detector*, Eur. Phys. J. C **77** (2017) 898, arXiv: 1708.03247 [hep-ex].

[30] ATLAS Collaboration, *ATLAS Run 1 searches for direct pair production of third-generation squarks at the Large Hadron Collider*, Eur. Phys. J. C **75** (2015) 510, arXiv: 1506.08616 [hep-ex].

[31] CMS Collaboration, *Searches for new phenomena in events with jets and high values of the* M_{T2} *variable, including signatures with disappearing tracks, in proton-proton collisions at* $\sqrt{s}$ = 13 TeV, Eur. Phys. J. C **80** (2020), arXiv: 1909.03460 [hep-ex].

[32] CMS Collaboration, *Search for direct production of supersymmetric partners of the top quark in the all-jets final state in proton-proton collisions at* $\sqrt{s}$ = 13 *TeV*, JHEP **10** (2017) 005, arXiv: 1707.03316 [hep-ex].

[33] CMS Collaboration, *Search for top squark pair production in pp collisions at* $\sqrt{s}$ = 13 *TeV using single lepton events*, JHEP **10** (2017) 019, arXiv: 1706.04402 [hep-ex].

[34] CMS Collaboration, *Search for top squarks and dark matter particles in opposite-charge dilepton final states at* $\sqrt{s}$ = *13 TeV*, Phys. Rev. D **97** (2018) 032009, arXiv: 1711.00752 [hep-ex].

[35] CMS Collaboration, *Searches for pair production of third-generation squarks in* $\sqrt{s}$ = 13 *TeV pp collisions*, Eur. Phys. J. C **77** (2017) 327, arXiv: 1612.03877 [hep-ex].

[36] CMS Collaboration, *A search for new phenomena in pp collisions at* $\sqrt{s}$ = 13 *TeV in final states with missing transverse momentum and at least one jet using the* α_T *variable*, Eur. Phys. J. C **77** (2017) 294, arXiv: 1611.00338 [hep-ex].

[37] CMS Collaboration, *Inclusive search for supersymmetry using razor variables in pp collisions at* $\sqrt{s}$ = 13 *TeV*, Phys. Rev. D **95** (2017) 012003, arXiv: 1609.07658 [hep-ex].

[38] CMS Collaboration, *Search for direct top squark pair production in events with one lepton, jets and missing transverse energy at* $\sqrt{s}$ = 13 TeV, CMS-PAS-SUS-19-009, 2019, URL: https://cds.cern.ch/record/2682157.

[39] ATLAS Collaboration, *Search for dark matter produced in association with bottom or top quarks in* $\sqrt{s}$ = *13 TeV pp collisions with the ATLAS detector*, Eur. Phys. J. C **2017** (2017), arXiv: 1710.11412 [hep-ex].

[40] CMS Collaboration, *Search for dark matter produced in association with heavy-flavor quark pairs in proton–proton collisions at* $\sqrt{s}$ = 13 *TeV*, Eur. Phys. J. C **77** (2017) 845, arXiv: 1706.02581 [hep-ex].

[41] J. Alwall, M.-P. Le, M. Lisanti and J. G. Wacker, *Searching for Directly Decaying Gluinos at the Tevatron*, Phys. Lett. B **666** (2008) 34, arXiv: 0803.0019.

[42] J. Alwall, P. Schuster and N. Toro, *Simplified Models for a First Characterization of New Physics at the LHC*, Phys. Rev. D **79** (2009) 075020, arXiv: 0810.3921.

[43] D. Alves et al., *Simplified Models for LHC New Physics Searches*, J. Phys. G **39** (2012) 105005, arXiv: 1105.2838.

[44] D. Abercrombie et al., *Dark Matter Benchmark Models for Early LHC Run-2 Searches: Report of the ATLAS/CMS Dark Matter Forum*, Phys. Dark Univ. **26** (2015) 100371, arXiv: 1507.00966 [hep-ex].

[45] ATLAS Collaboration, *Search for direct top squark pair production in the 3-body decay mode with a final state containing one lepton, jets and missing transverse momentum in* $\sqrt{s}$ = 13 *TeV pp collision data with the ATLAS detector*, ATLAS-CONF-2019-017, 2019, URL: https://cds.cern.ch/record/2676594.

[46] ATLAS Collaboration, *The ATLAS Experiment at the CERN Large Hadron Collider*, JINST **3** (2008) S08003.

[47] ATLAS Collaboration, *ATLAS Insertable B-Layer Technical Design Report*, ATLAS-TDR-19, 2010, URL: https://cds.cern.ch/record/1291633,
ATLAS Insertable B-Layer Technical Design Report Addendum, ATLAS-TDR-19-ADD-1, 2012, URL: https://cds.cern.ch/record/1451888.

[48] ATLAS IBL Collaboration, *Production and Integration of the ATLAS Insertable B-Layer*, JINST **13** (2018) T05008, arXiv: 1803.00844 [physics.ins-det].

[49] ATLAS Collaboration, *Optimisation of the ATLAS b-tagging performance for the 2016 LHC Run*, ATL-PHYS-PUB-2016-012, 2016, URL: https://cds.cern.ch/record/2160731.

[50] ATLAS Collaboration, *Performance of the ATLAS Trigger System in 2015*, Eur. Phys. J. C **77** (2017) 317, arXiv: 1611.09661 [hep-ex].

[51] ATLAS Collaboration,
Luminosity determination in pp collisions at $\sqrt{s} = 8$ TeV using the ATLAS detector at the LHC, Eur. Phys. J. C **76** (2016) 653, arXiv: 1608.03953 [hep-ex].

[52] G. Avoni et al., *The new LUCID-2 detector for luminosity measurement and monitoring in ATLAS*, JINST **13** (2018) P07017.

[53] S. Alioli, P. Nason, C. Oleari and E. Re, *A general framework for implementing NLO calculations in shower Monte Carlo programs: the POWHEG BOX*, JHEP **06** (2010) 043, arXiv: 1002.2581 [hep-ph].

[54] R. D. Ball et al., *Parton distributions for the LHC Run II*, JHEP **04** (2015) 040, arXiv: 1410.8849 [hep-ph].

[55] T. Sjöstrand, S. Mrenna and P. Z. Skands, *A Brief Introduction to PYTHIA 8.1*, Comput. Phys. Commun. **178** (2008) 852, arXiv: 0710.3820 [hep-ph].

[56] ATLAS Collaboration, *ATLAS Pythia 8 tunes to 7 TeV data*, ATL-PHYS-PUB-2014-021, 2014, URL: https://cds.cern.ch/record/1966419.

[57] M. Czakon, P. Fiedler and A. Mitov,
Total Top-Quark Pair-Production Cross Section at Hadron Colliders Through $O(\alpha_S^4)$, Phys. Rev. Lett. **110** (2013) 252004, arXiv: 1303.6254 [hep-ph].

[58] M. Czakon and A. Mitov,
NNLO corrections to top pair production at hadron colliders: the quark-gluon reaction, JHEP **01** (2013) 080, arXiv: 1210.6832 [hep-ph].

[59] M. Czakon and A. Mitov, *NNLO corrections to top-pair production at hadron colliders: the all-fermionic scattering channels*, JHEP **12** (2012) 054, arXiv: 1207.0236 [hep-ph].

[60] P. Bärnreuther, M. Czakon and A. Mitov, *Percent Level Precision Physics at the Tevatron: First Genuine NNLO QCD Corrections to $q\bar{q} \to t\bar{t} + X$*, Phys. Rev. Lett. **109** (2012) 132001, arXiv: 1204.5201 [hep-ph].

[61] M. Cacciari, M. Czakon, M. Mangano, A. Mitov and P. Nason, *Top-pair production at hadron colliders with next-to-next-to-leading logarithmic soft-gluon resummation*, Phys. Lett. B **710** (2012) 612, arXiv: 1111.5869 [hep-ph].

[62] M. Czakon and A. Mitov,
Top++: A Program for the Calculation of the Top-Pair Cross-Section at Hadron Colliders, Comput. Phys. Commun. **185** (2014) 2930, arXiv: 1112.5675 [hep-ph].

[63] N. Kidonakis, *Next-to-next-to-leading-order collinear and soft gluon corrections for t-channel single top quark production*, Phys. Rev. D **83** (2011) 091503, arXiv: 1103.2792 [hep-ph].

[64] N. Kidonakis, *Two-loop soft anomalous dimensions for single top quark associated production with a W- or H-*, Phys. Rev. D **82** (2010) 054018, arXiv: 1005.4451 [hep-ph].

[65] N. Kidonakis, *NNLL resummation for s-channel single top quark production*, Phys. Rev. D **81** (2010) 054028, arXiv: 1001.5034 [hep-ph].

[66] T. Gleisberg et al., *Event generation with SHERPA 1.1*, JHEP **02** (2009) 007, arXiv: 0811.4622 [hep-ph].

[67] S. Catani, L. Cieri, G. Ferrera, D. de Florian and M. Grazzini, *Vector boson production at hadron colliders: a fully exclusive QCD calculation at NNLO*, Phys. Rev. Lett. **103** (2009) 082001, arXiv: 0903.2120 [hep-ph].

[68] J. Alwall et al., *The automated computation of tree-level and next-to-leading order differential cross sections, and their matching to parton shower simulations*, JHEP **07** (2014) 079, arXiv: 1405.0301 [hep-ph].

[69] R. D. Ball et al., *Parton distributions with LHC data*, Nucl. Phys. B **867** (2013) 244, arXiv: 1207.1303 [hep-ph].

[70] M. Beneke, M. Czakon, P. Falgari, A. Mitov and C. Schwinn, *Threshold expansion of the $gg(q\bar{q}) \to Q\bar{Q} + X$ cross section at $O(\alpha_s^4)$*, Phys. Lett. B **690** (2010) 483, arXiv: 0911.5166 [hep-ph], Erratum: Phys. Lett. B **778** (2018) 464.

[71] M. Beneke, M. Czakon, P. Falgari, A. Mitov and C. Schwinn, Phys. Lett. B **778** (2018) 464.

[72] W. Beenakker, C. Borschensky, M. Krämer, A. Kulesza and E. Laenen, *NNLL-fast: predictions for coloured supersymmetric particle production at the LHC with threshold and Coulomb resummation*, JHEP **12** (2016) 133, arXiv: 1607.07741 [hep-ph].

[73] O. Mattelaer and E. Vryonidou, *Dark matter production through loop-induced processes at the LHC: the s-channel mediator case*, Eur. Phys. J. C **75** (2015) 436, arXiv: 1508.00564 [hep-ph].

[74] M. Backovic et al., *Higher-order QCD predictions for dark matter production at the LHC in simplified models with s-channel mediators*, Eur. Phys. J. C **75** (2015) 482, arXiv: 1508.05327 [hep-ph].

[75] E. Re, *Single-top Wt-channel production matched with parton showers using the POWHEG method*, Eur. Phys. J. C **71** (2011) 1547, arXiv: 1009.2450 [hep-ph].

[76] S. Frixione, P. Nason and G. Ridolfi, *A Positive-weight next-to-leading-order Monte Carlo for heavy flavour hadroproduction*, JHEP **09** (2007) 126, arXiv: 0707.3088 [hep-ph].

[77] R. Frederix, E. Re and P. Torrielli, *Single-top t-channel hadroproduction in the four-flavour scheme with POWHEG and aMC@NLO*, JHEP **09** (2012) 130, arXiv: 1207.5391 [hep-ph].

[78] S. Alioli, P. Nason, C. Oleari and E. Re, *NLO single-top production matched with shower in POWHEG: s- and t-channel contributions*, JHEP **09** (2009) 111, Erratum: JHEP 02 (2010) 011, arXiv: 0907.4076 [hep-ph].

[79] D. J. Lange, *The EvtGen particle decay simulation package*, Nucl. Instrum. Meth. A **462** (2001) 152.

[80] ATLAS Collaboration, *The ATLAS Simulation Infrastructure*, Eur. Phys. J. C **70** (2010) 823, arXiv: 1005.4568 [physics.ins-det].

[81] S. Agostinelli et al. (GEANT4 Collaboration), *GEANT4: A Simulation toolkit*, Nucl. Instrum. Meth. A **506** (2003) 250.

[82] ATLAS Collaboration, *The Pythia 8 A3 tune description of ATLAS minimum bias and inelastic measurements incorporating the Donnachie–Landshoff diffractive model*, ATL-PHYS-PUB-2016-017, 2016, URL: https://cds.cern.ch/record/2206965.

[83] M. Bahr et al., *Herwig++ Physics and Manual*, Eur. Phys. J. C **58** (2008) 639, arXiv: 0803.0883 [hep-ph].

[84] J. Bellm et al., *Herwig 7.0/Herwig++ 3.0 release note*, Eur. Phys. J. C **76** (2016) 196, arXiv: 1512.01178 [hep-ph].

[85] ATLAS Collaboration, *Studies on top-quark Monte Carlo modelling with Sherpa and MG5_ aMC@NLO*, ATL-PHYS-PUB-2017-007, 2017, URL: https://cds.cern.ch/record/2261938.

[86] S. Frixione, E. Laenen, P. Motylinski, B. R. Webber and C. D. White, *Single-top hadroproduction in association with a W boson*, JHEP **07** (2008) 029, arXiv: 0805.3067 [hep-ph].

[87] ATLAS Collaboration, *Probing the Quantum Interference between Singly and Doubly Resonant Top-Quark Production in p-p Collisions at* $\sqrt{s} = 13$ *TeV with the ATLAS Detector*, Phys. Rev. Lett. **121** (2018) 152002, arXiv: 1806.04667 [hep-ex].

[88] ATLAS Collaboration, *ATLAS simulation of boson plus jets processes in Run 2*, ATL-PHYS-PUB-2017-006, 2017, URL: https://cds.cern.ch/record/2261937.

[89] ATLAS Collaboration, *Multiboson simulation for* 13 *TeV ATLAS analyses*, ATL-PHYS-PUB-2017-005, 2017, URL: https://cds.cern.ch/record/2261933.

[90] T. Gleisberg and S. Höche, *Comix, a new matrix element generator*, JHEP **12** (2008) 039, arXiv: 0808.3674 [hep-ph].

[91] F. Cascioli, P. Maierhofer and S. Pozzorini, *Scattering Amplitudes with Open Loops*, Phys. Rev. Lett. **108** (2012) 111601, arXiv: 1111.5206 [hep-ph].

[92] S. Schumann and F. Krauss, *A Parton shower algorithm based on Catani-Seymour dipole factorisation*, JHEP **03** (2008) 038, arXiv: 0709.1027 [hep-ph].

[93] S. Höche, F. Krauss, M. Schönherr and F. Siegert, *QCD matrix elements + parton showers: The NLO case*, JHEP **04** (2013) 027, arXiv: 1207.5030 [hep-ph].

[94] ATLAS Collaboration, *Modelling of the* $t\bar{t}H$ *and* $t\bar{t}V(V = W, Z)$ *processes for* $\sqrt{s} = 13$ *TeV ATLAS analyses*, ATL-PHYS-PUB-2016-005, 2016, URL: https://cds.cern.ch/record/2120826.

[95] P. Artoisenet, R. Frederix, O. Mattelaer and R. Rietkerk, *Automatic spin-entangled decays of heavy resonances in Monte Carlo simulations*, JHEP **03** (2013) 015, arXiv: 1212.3460 [hep-ph].

[96] W. Beenakker, M. Kramer, T. Plehn, M. Spira and P. M. Zerwas, *Stop production at hadron colliders*, Nucl. Phys. B **515** (1998) 3, arXiv: hep-ph/9710451 [hep-ph].

[97] W. Beenakker et al., *Supersymmetric top and bottom squark production at hadron colliders*, JHEP **08** (2010) 098, arXiv: 1006.4771.

[98] W. Beenakker et al., *NNLL resummation for stop pair-production at the LHC*, JHEP **05** (2016) 153, arXiv: 1601.02954 [hep-ph].

[99] J. Butterworth et al., *PDF4LHC recommendations for LHC Run II*, J. Phys. G **43** (2016) 023001, arXiv: 1510.03865 [hep-ph].

[100] ATLAS Collaboration, *Electron and photon performance measurements with the ATLAS detector using the 2015-2017 LHC proton-proton collision data*, JINST **14** (2019) P12006, arXiv: 1908.00005 [hep-ex].

[101] ATLAS Collaboration, *Muon reconstruction performance of the ATLAS detector in proton–proton collision data at* $\sqrt{s} = 13$ *TeV*, Eur. Phys. J. C **76** (2016) 292, arXiv: 1603.05598 [hep-ex].

[102] ATLAS Collaboration, *Topological cell clustering in the ATLAS calorimeters and its performance in LHC Run 1*, Eur. Phys. J. C **77** (2017) 490, arXiv: 1603.02934 [hep-ex].

[103] ATLAS Collaboration, *Jet energy measurement with the ATLAS detector in proton–proton collisions at* $\sqrt{s} = 7$ *TeV*, Eur. Phys. J. C **73** (2013) 2304, arXiv: 1112.6426 [hep-ex].

[104] M. Cacciari, G. P. Salam and G. Soyez, *The Anti-k(t) jet clustering algorithm*, JHEP **04** (2008) 063, arXiv: 0802.1189 [hep-ph].

[105] M. Cacciari, G. P. Salam and G. Soyez, *FastJet User Manual*, Eur. Phys. J. **C72** (2012) 1896, arXiv: 1111.6097 [hep-ph].

[106] M. Cacciari and G. P. Salam, *Pileup subtraction using jet areas*, Phys. Lett. B **659** (2008) 119, arXiv: 0707.1378 [hep-ph].

[107] M. Cacciari, G. P. Salam and G. Soyez, *The Catchment Area of Jets*, JHEP **04** (2008) 005, arXiv: 0802.1188 [hep-ph].

[108] ATLAS Collaboration, *Performance of pile-up mitigation techniques for jets in pp collisions at* $\sqrt{s} = 8$ *TeV using the ATLAS detector*, Eur. Phys. J. C **76** (2016) 581, arXiv: 1510.03823 [hep-ex].

[109] ATLAS Collaboration, *Jet energy measurement and its systematic uncertainty in proton–proton collisions at* $\sqrt{s} = 7$ *TeV with the ATLAS detector*, Eur. Phys. J. C **75** (2015) 17, arXiv: 1406.0076 [hep-ex].

[110] ATLAS Collaboration, *Jet energy scale measurements and their systematic uncertainties in proton–proton collisions at* $\sqrt{s} = 13$ *TeV with the ATLAS detector*, Phys. Rev. D **96** (2017) 072002, arXiv: 1703.09665 [hep-ex].

[111] ATLAS Collaboration, *Characterisation and mitigation of beam-induced backgrounds observed in the ATLAS detector during the 2011 proton–proton run*, JINST **8** (2013) P07004, arXiv: 1303.0223 [hep-ex].

[112] ATLAS Collaboration,
Selection of jets produced in 13 *TeV proton–proton collisions with the ATLAS detector*,
ATLAS-CONF-2015-029, 2015, URL: https://cds.cern.ch/record/2037702.

[113] ATLAS Collaboration, *Performance of b-Jet Identification in the ATLAS Experiment*,
JINST **11** (2016) P04008, arXiv: 1512.01094 [hep-ex].

[114] ATLAS Collaboration, *ATLAS b-jet identification performance and efficiency measurement with tt events in pp collisions at 13 TeV*, Eur. Phys. J. C **79** (2019) 970, arXiv: 1907.05120 [hep-ex].

[115] ATLAS Collaboration, *Soft b-hadron tagging for compressed SUSY scenarios*,
ATLAS-CONF-2019-027, 2019, URL: http://cdsweb.cern.ch/record/2682131.

[116] ATLAS Collaboration, *Measurement of the tau lepton reconstruction and identification performance in the ATLAS experiment using pp collisions at* $\sqrt{s}$ = 13 *TeV*,
ATLAS-CONF-2017-029, 2017, URL: https://cds.cern.ch/record/2261772.

[117] ATLAS Collaboration,
Reconstruction of hadronic decay products of tau leptons with the ATLAS experiment,
Eur. Phys. J. C **76** (2016) 295, arXiv: 1512.05955 [hep-ex].

[118] ATLAS Collaboration, *Modelling* $Z \to \tau\tau$ *processes in ATLAS with* τ*-embedded* $Z \to \mu\mu$ *data*,
JINST **10** (2015) P09018, arXiv: 1506.05623 [hep-ex].

[119] ATLAS Collaboration, *Identification and energy calibration of hadronically decaying tau leptons with the ATLAS experiment in pp collisions at* $\sqrt{s}$ = 8 *TeV*, Eur. Phys. J. C **75** (2015) 303,
arXiv: 1412.7086 [hep-ex].

[120] ATLAS Collaboration, *Performance of missing transverse momentum reconstruction with the ATLAS detector using proton–proton collisions at* $\sqrt{s}$ = 13 *TeV*, Eur. Phys. J. C **78** (2018) 903,
arXiv: 1802.08168 [hep-ex].

[121] ATLAS Collaboration,
E_T^{miss} *performance in the ATLAS detector using 2015–2016 LHC pp collisions*,
ATLAS-CONF-2018-023, 2018, URL: https://cds.cern.ch/record/2625233.

[122] C. G. Lester and D. J. Summers,
Measuring masses of semi-invisibly decaying particles pair produced at hadron colliders,
Phys. Lett. B **463** (1999) 99, arXiv: hep-ph/9906349.

[123] ATLAS Collaboration,
Search for top squark pair production in final states with one isolated lepton, jets, and missing transverse momentum in $\sqrt{s}$ = 8 *TeV pp collisions with the ATLAS detector*, JHEP **11** (2014) 118,
arXiv: 1407.0583 [hep-ex].

[124] M. L. Graesser and J. Shelton, *Hunting mixed top squark decays*,
Phys. Rev. Lett. **111** (2013) 035031, arXiv: 1212.4495 [hep-ph].

[125] H. An and L.-T. Wang, *Opening up the compressed region of top squark searches at 13 TeV LHC*,
Phys. Rev. Lett. **115** (2015) 181602, arXiv: 1506.00653 [hep-ph].

[126] S. Macaluso, M. Park, D. Shih and B. Tweedie,
Revealing Compressed Stops Using High-Momentum Recoils, JHEP **03** (2016) 151,
arXiv: 1506.07885 [hep-ph].

[127] C. Borschensky et al.,
Squark and gluino production cross sections in pp collisions at $\sqrt{s}$ *= 13, 14, 33 and 100 TeV*,
Eur. Phys. J. C **74** (2014) 3174, arXiv: 1407.5066.

[128] R. D. Cousins, J. T. Linnemann and J. Tucker,
Evaluation of three methods for calculating statistical significance when incorporating a systematic uncertainty into a test of the background-only hypothesis for a Poisson process,
Nuclear Instruments and Methods in Physics Research A **595** (2008) 480,
arXiv: physics/0702156 [physics.data-an].

[129] A. L. Read, *Presentation of search results: The CL_s technique*, J. Phys. G **28** (2002) 2693.